8-21-2013

# Three-Dimensional Finite Element Analysis of Solid Oxide Fuel Cell Microstructures

Sushrut S. Vaidya
*University of Connecticut*, vaidya.sushrut@gmail.com

Three-Dimensional Finite Element Analysis of Solid Oxide Fuel Cell Microstructures

Sushrut Sanjiv Vaidya, Ph.D.

University of Connecticut, 2013

## Abstract

Finite element thermal stress analyses of solid oxide fuel cell (SOFC) electrode microstructure models are performed under various conditions to investigate mechanical integrity of electrodes under thermal loads. Image-based three-dimensional finite element models of electrode microstructures are generated from two-dimensional images of actual electrode cross-sections. Finite element thermal stress analyses of anode models under spatially uniform temperature fields of increasing magnitude are performed, and the effects of temperature-dependent material properties and plasticity on mechanical integrity are investigated. Linear elastic material models are found to underestimate the probability of failure of the anode at high temperatures. Analyses of cathode models are performed to study the effects of temperature-dependent material properties and varying phase volume fractions. An approximate heuristic scheme based on boundary pixel modification is developed, validated, and used to derive a microstructure of varying composition from the original microstructure. Limited variations in ceramic phase volume fractions are found to have limited effect on probability of failure of models having temperature-independent material properties, with higher pore volume fraction leading to higher probability of failure. Consideration of temperature-dependent material properties leads to lower probability of failure for the cathode models compared with temperature-independent material properties. Interface degradation under repeated thermal loading is simulated using cohesive elements. Effects of damage on mechanical integrity and electrochemical performance are studied. Three-phase boundary evolution due to mechanical interface damage is evaluated. Three-phase boundary density is found to decrease over a number of heating cycles, indicating that interface damage may be a major mechanism responsible for SOFC performance degradation over time.

# Three-Dimensional Finite Element Analysis of Solid Oxide Fuel Cell Microstructures

Sushrut Sanjiv Vaidya

B.E., University of Mumbai, Mumbai, India, 2005

M.Tech., Indian Institute of Technology Kharagpur, Kharagpur, India, 2008

A Dissertation

Submitted in Partial Fulfillment of the

Requirements for the Degree of Doctor of Philosophy

at the

University of Connecticut

2013

APPROVAL PAGE

Doctor of Philosophy Dissertation

Three-Dimensional Finite Element Analysis of Solid Oxide Fuel Cell Microstructures

Presented by

Sushrut Sanjiv Vaidya, B.E., M.Tech.

Major Advisor _____

Jeong-Ho Kim

Associate Advisor _____

Michael L. Accorsi

Associate Advisor _____

Ramesh B. Malla

University of Connecticut

2013

## ACKNOWLEDGMENTS

I would like to express my sincere gratitude for the guidance and help provided by Prof. Jeong-Ho Kim, my Major Advisor. The work presented in this dissertation would not have been possible without the encouragement, motivation, and insights provided by Prof. Kim. I would also like to thank my Associate Advisors, Prof. Michael L. Accorsi and Prof. Ramesh B. Malla, for their guidance, helpful comments, and support. The insights provided by Prof. Kim, Prof. Accorsi, and Prof. Malla have enriched not only the contents of this dissertation but also my entire experience as a doctoral student at the University of Connecticut. I sincerely thank all the faculty members of the Structures and Applied Mechanics group within the Department of Civil and Environmental Engineering for providing an excellent environment for academic activities. I would like to thank the entire administrative staff of the office of the Civil and Environmental Engineering Department for providing outstanding administrative support. I thank all my fellow graduate students for their support and for providing an intellectually challenging academic environment. The financial support for this work received from the National Science Foundation under the Faculty Early Career Development (CAREER) Grant CMMI-0546225 (Material Design & Surface Engineering Program) awarded to Prof. Kim is gratefully acknowledged. I would also like to thank the Department of Civil and Environmental Engineering for financially supporting part of my doctoral studies at the University of Connecticut. The assistance received from the research group of Dr. Scott Barnett at the Department of Materials Science and Engineering at Northwestern University, Evanston, Illinois is acknowledged with thanks. They shared their research in the form of two-dimensional images of anode and cathode microstructures. The constant moral support provided by my wife, Sudha Srinivasan, has been invaluable. My doctoral work would have been impossible to complete without her constant encouragement. I sincerely thank our families in India, who have supported us throughout our stay at the University of Connecticut. Their best wishes and prayers have played a big role in the completion of this work.

## Table of Contents

## List of Tables

## List of Figures

# Chapter 1

# Introduction to Solid Oxide Fuel Cells

## 1.1. Introduction

A solid oxide fuel cell (SOFC) is an electrochemical power source that converts the chemical energy of fuels into electrical energy [1]. SOFCs have received attention from researchers due to their promise of delivering relatively clean energy at high efficiencies [1]. An SOFC consists of anode, cathode, electrolyte, and interconnect wires [1]. The electrolyte is a solid oxide such as yttria-stabilized zirconia (YSZ). The porous anode is a ceramic-metal composite ('cermet') of nickel and zirconia (Ni-YSZ). The porous cathode is a composite of ceramic materials such as strontium-doped lanthanum manganite and yttria-stabilized zirconia (LSM-YSZ) [1]. Oxygen atoms undergo reduction on the porous cathode surface, and the resulting oxide ions are transported through the electrolyte to the porous anode. Here, the oxide ions react with the fuel (e.g. hydrogen). Hydrogen is oxidized, and the electrons of the oxide ions are liberated. The free electrons give rise to electric current [1]. Typical SOFC operating temperatures lie in the range of 600 – 1000 $^{0}$C [1]. This process is schematically illustrated in Figure 1-1.

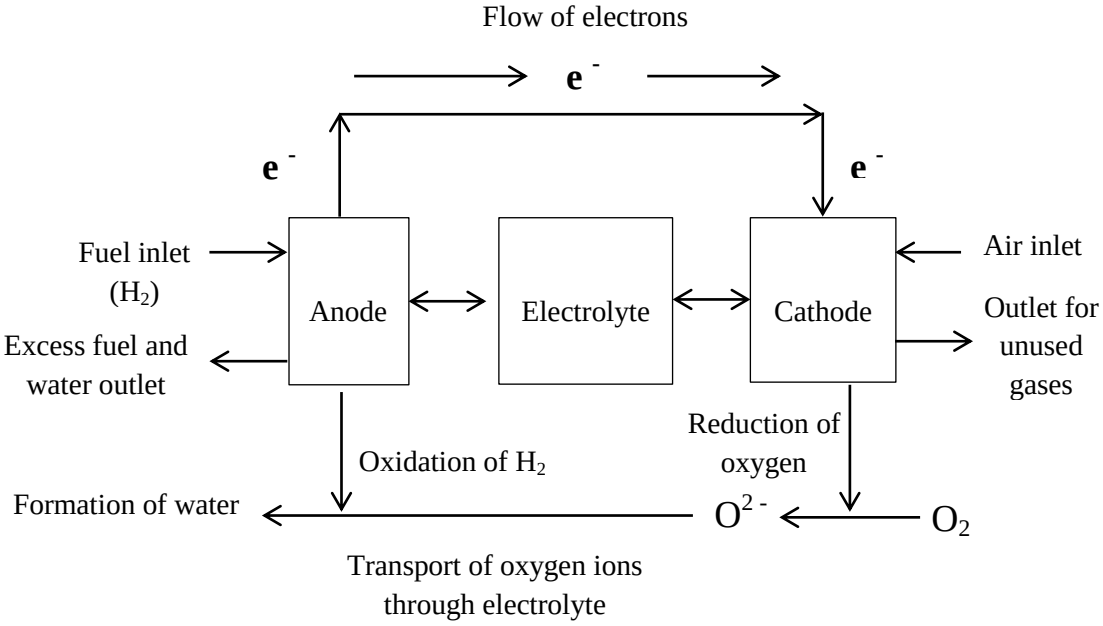


**Figure 1-1** Schematic diagram of solid oxide fuel cell

The potential uses of SOFCs include both stationary applications (e.g. residential power generation) and mobile applications (e.g. auxiliary power units in automobiles). Their main advantages are high efficiency, fuel flexibility, and low emissions [1]. The main disadvantage of SOFCs is the high operating temperature, which leads to durability and mechanical integrity issues during thermal cycling [1]. Thus, a major objective of current SOFC research activity is to reduce the operating temperature, which may potentially increase the service life of the cell and make the technology applicable on a large scale [1].

### 1.2. Review of literature on electrochemical and mechanical aspects of SOFC

Researchers have investigated many different aspects of SOFCs, including anode, cathode, and electrolyte materials; behavior of different SOFC configurations; modeling of electrochemical, thermal, and flow phenomena; and probability of failure under thermal loads. Due to the relatively high operating temperatures ($600 - 1000^0$C), thermal stresses significantly impact the mechanical integrity of the SOFC [2, 3]. Research has also established that electrochemical performance of SOFCs is significantly affected by component microstructure [4, 5]. Recently, a preliminary investigation [6] has been undertaken to study the effects of SOFC anode microstructure on thermal stresses induced by a temperature field.

Experimental, analytical, and computational approaches have been used to investigate the properties of materials used in SOFC and to study the electrochemical and mechanical behavior of SOFC. Selcuk and Atkinson [7, 8] conducted a number of experimental studies to estimate various mechanical properties of SOFC ceramic materials such as YSZ and NiO-YSZ. They determined the biaxial flexural strength and fracture toughness of YSZ at room temperature and at an operating temperature of $900^0$C [8]. They also experimentally studied the dependence of the Young's modulus, shear modulus, and Poisson's ratio of YSZ and NiO-YSZ (amongst other ceramic materials) on porosity [7]. The results of these studies were summarized by Atkinson and Selcuk [9], where they also suggested techniques for improving the mechanical behavior of SOFC ceramic materials under certain operating conditions. Toftegaard *et al.* [10] conducted uniaxial tensile tests on pure YSZ specimens and YSZ specimens coated with porous NiO-YSZ layers. They heat-treated the coated YSZ specimens at various temperatures to study the effect of

heat treatment at different temperatures on the strength. Pihlatie *et al.* [11] experimentally determined the Young's modulus (amongst other mechanical properties) of Ni-YSZ and NiO-YSZ composites as a function of porosity using the Impulse Excitation Technique (IET). They also used IET to study the dependency of the Young's modulus of these materials on temperature. Giraud and Canel [12] also conducted experimental studies using IET to determine the variation of the Young's modulus of YSZ, LSM, and Ni-YSZ with temperature.

Zhang *et al.* [13] developed an analytical model for calculating residual stresses in a single SOFC with NiO-YSZ/YSZ/LSM composition, using effective material properties. They used their model to estimate the residual stresses in an SOFC at room temperature and to study the variation of the stresses in the different components with changes in component thickness. They also performed Weibull analysis to calculate the probability of failure of the anode. They investigated the variation of the probability of failure of the anode with changes in component thickness. Selimovic *et al*. [2] developed a finite element (FE) model of a planar SOFC, without considering microstructure, to study mechanical stresses under steady-state and transient thermal loads. Anandakumar *et al.* [3] carried out finite element analysis (FEA) to estimate thermal stresses and probability of failure in functionally graded SOFCs. However, they did not consider the microstructure of the SOFC components in their models. Instead, they used graded finite elements to discretize effective media. They also used the Weibull method to estimate the probability of failure of the individual components of the SOFC, as well as that of the whole SOFC. Anandakumar *et al.* [3] found that the thermal stresses developed in functionally graded SOFCs under spatially uniform and non-uniform temperature loads are lower than those induced in conventional layered SOFCs. They also found that functionally graded SOFCs show a lower probability of failure than other types of SOFCs.

Laurencin *et al.* [14] conducted FEA to study the degradation of anode-supported and electrolyte-supported circular planar SOFCs under several types of mechanical loads, including residual stresses. They also calculated the probability of failure of the SOFCs using Weibull analysis. However, they considered only elastic behavior. Pitakthapanaphong and Busso [15] carried out FEA to investigate the

fracture of multi-layered systems used in SOFCs, and noted that fracture is caused by large residual stresses induced during the SOFC manufacturing process due to thermal expansion coefficient (TEC) mismatch between different layers. They observed different cracking patterns (surface cracks, channeling cracks, and interfacial cracks) in physical samples of multi-layered systems. Their study involved simulations using FE models of multi-layered samples to determine the crack driving force (energy release rate) for the three observed cracking patterns. However, they did not consider the microstructure of the multi-layered systems. Johnson and Qu [16] used a three-dimensional stochastic reconstruction method to create multiple realizations of the microstructure of porous Ni-YSZ cermet used as SOFC anode material. They analyzed these microstructure realizations using finite element software to determine the effective elastic modulus and effective coefficient of thermal expansion (CTE) of Ni-YSZ as a function of temperature. Liu *et al.* [17] studied the strength of SOFC ceramic electrodes with high porosity using discrete element simulations. They investigated the elastic and fracture behavior of such electrodes and proposed an Orowan-Petch type relation between fracture strength and particle size. Clague *et al.* [6] used focused ion beam (FIB) tomography to obtain detailed images of Ni-YSZ electrode microstructure. They developed and analyzed a finite element model of the electrode microstructure using commercially available software. The authors simulated the heating of the microstructure from room temperature to operating temperature by applying a temperature field, and conducted implicit linear elastic FE analysis to determine stresses. Finally, it is worth mentioning that numerical simulation activities in the field of SOFC research have produced a significant volume of technical literature. A detailed overview of the field of numerical modeling of SOFCs is provided by Kakac *et al.* in their review paper [18].

## 1.3. Motivation and objectives

### *1.3.1. Motivation for research*

From the review of literature presented in the previous section, it can be observed that although the effects of microstructure on SOFC electrochemical performance have been investigated, and mechanical performance under thermal loads has been studied using effective media, relatively few investigations have focused on the effects of microstructure on mechanical performance [6]. Mechanical durability of the SOFC under steady-state and transient thermal loads is an important aspect of performance. It is thus essential to understand the effects of microstructure on probability of failure under thermal loads. Most computational studies have employed effective material properties and have modeled the SOFC components as effective media. They have not directly modeled the microstructure of the components. Also, the effects of temperature-dependent material properties, elastic-plastic behavior and electrode composition on mechanical integrity have not been extensively studied. Electrode degradation has not been simulated in conjunction with microstructure-based FE models in the literature. These observations provide the motivation for the work presented in this document. Several key areas within the field of finite element thermal stress analysis of SOFC electrodes are identified and listed below. The volume of literature in these areas appears to be insufficient, and the objective of the research presented in this dissertation is to address some of these gaps in the present state of knowledge of the behavior of SOFC under thermal loads.

*a. Component microstructure*

It is clear from the previous discussion that microstructure plays a very important role in determining the electrochemical and mechanical behavior of SOFC components. It is important to consider microstructure in thermal stress and probability of failure analyses of SOFC electrodes in order to account for the stress concentration effects of pores.

*b. Temperature-dependent material properties*

Given the high operating temperatures of solid oxide fuel cells (600 – 1000ºC) and the occurrence of thermal cycling during operation, it is very important to consider variation of material properties with temperature in investigating the mechanical integrity of SOFC under thermal loads.

*c. Elastic-plastic behavior*

It is necessary to consider plastic behavior of the nickel phase of Ni-YSZ anodes at high temperatures. Clague *et al.* [6] have pointed out that plastic behavior of nickel may provide a mechanism for stress relief in anodes.

*d. Effects of electrode composition*

In practice, SOFC electrodes possess varying phase compositions in the thickness direction [1]. This variation increases material compatibility between different SOFC components and improves overall cell performance. Construction of microstructures with different phase volume fractions may provide physical insights into the effects of varying phase compositions on the mechanics of electrode structures in SOFC.

*e. Effects of electrode degradation*

Solid oxide fuel cells are subjected to thermal cycling as well as redox cycling. Such cyclic operation, combined with stress concentration due to the porous microstructures of the electrodes, may cause damage initiation and evolution in the SOFC structure [17]. In order to improve the understanding of the behavior of SOFC under thermal loads, it is essential to incorporate a realistic damage evolution scheme into microstructure-based finite element models.

The motivation for the present research is provided by the need to address the above gaps in the body of knowledge on SOFC behavior under thermal loads. The specific objectives of the present work are stated in the following subsection.

*1.3.2. Objectives of research*

In order to address the issues identified in the previous subsection, specific objectives have been formulated for this research. The objectives of the research presented in this document are listed below.

***Objective 1:*** *Generation of three-dimensional finite element models of SOFC electrode microstructures*

This objective involves the generation of three-dimensional (3-D) FE models of SOFC anode and cathode microstructures from a set of two-dimensional microstructure images [19, 20] using in-house computer programs.

***Objective 2:*** *Finite element thermal stress analysis of SOFC microstructures considering temperature-dependent material properties*

This objective involves finite element analysis (FEA) of the electrode microstructure models considering temperature-independent and temperature-dependent material properties to determine stresses induced by a steady-state temperature change from room temperature up to operating temperature. The thermal stresses obtained from FEA are analyzed using the Weibull method [21] to calculate the probability of failure. The effects of temperature-independent versus temperature-dependent material properties are studied for both anode and cathode microstructures.

***Objective 3:*** *Investigation of the effects of plasticity on the behavior of the anode microstructure under thermal loads*

The effects of plasticity on the probability of failure of the anode microstructure under thermal loads are studied. This objective involves consideration of elastic-plastic behavior of the nickel phase, in addition to temperature-dependent material properties, for the anode microstructure.

***Objective 4:*** *Investigation of the effects of varying phase compositions on the behavior of the cathode microstructure under thermal loads*

The effects of varying phase volume fractions on the probability of failure of the cathode microstructure under thermal loads are studied. This objective involves consideration of two different compositions for the cathode microstructure, in addition to temperature-dependent material properties.

***Objective 5:*** *Investigation of the effects of interface degradation on the behavior of electrode microstructures under repeated thermal loads*

Interface degradation in the electrode microstructures due to high temperatures and thermal cycling is simulated by considering imperfect bonding between dissimilar solid phases, using cohesive elements. A simplified interface damage scheme is implemented in the finite element microstructure models to simulate the effects of progressive degradation of interface strength and fracture energy. The effects of electrochemical reactions and redox cycling on interface degradation are not considered in this work.

### 1.4. Organization of the dissertation

Chapter 1 introduces certain basic aspects of SOFCs and presents a brief review of the technical literature on this subject. It also explains the motivation for this research and its objectives. The models, methods, and techniques used for achieving the objectives are explained in detail in Chapters 2, 3, and 4 of this work. Chapter 2 covers generation of 3-D, image-based, FE microstructure anode models and investigation of the effects of temperature-dependent material properties and plasticity (Objectives 1, 2, and 3). Chapter 3 describes generation of 3-D FE cathode microstructure models and investigation of the effects of temperature-dependent material properties and varying phase volume fractions on the behavior of the cathode microstructure under thermal loads (Objectives 1, 2, and 4). Chapter 4 investigates the effects of interface degradation under repeated thermal loading on the behavior of SOFC electrode microstructures (Objective 5). Mechanical degradation under repeated thermal loading is studied using energy concepts from fracture mechanics. Electrochemical performance degradation over time is

evaluated in a simplified manner by determining the evolution of three-phase boundaries (TPBs) with thermal cycling. The dissertation concludes with Chapter 5, which summarizes the main results and limitations of the work and suggests topics for future research.

# Chapter 2

# Finite Element Thermal Stress Analysis of SOFC Anode Microstructures: Effects of Material Nonlinearity and Temperature-Dependent Material Properties

## 2.1. Introduction

In this chapter, three-dimensional finite element (FE) models of solid oxide fuel cell (SOFC) anode microstructures are generated from a stack of two-dimensional microstructural images. Finite element analysis (FEA) of the anode microstructure models is carried out to determine thermal stresses induced by a steady-state temperature change from room temperature up to operating temperature. The stresses are analyzed using the Weibull method [21] to calculate the probability of failure. The anode material is 50:50 weight percentage (wt. %) Ni-YSZ. Both linear elastic and elastic-plastic (nonlinear) behaviors are considered for nickel (Ni) in the analyses. The effect of temperature-dependent material properties on the probability of failure of the anode is also investigated. The novelties of this work include FE analysis of the behavior of microstructure-based anode models under thermal loads considering temperature-dependent material properties and nonlinear (elastic-plastic) behavior of the nickel phase [22].

## 2.2. Image-based finite element anode microstructure models

The first step in this work involves reconstruction of a three-dimensional (3-D) anode microstructure from two-dimensional (2-D) images of anode cross-sections obtained using focused ion beam-scanning electron microscopy (FIB-SEM). The 2-D images of the anode microstructures have been obtained from Dr. Scott Barnett's research group at Northwestern University [19]. The initial 3-D reconstruction is achieved using IMOD [23], a free collection of image processing programs developed by researchers at the Boulder Laboratory for 3-D Electron Microscopy of Cells. IMOD is capable of creating a stack of 2-D images, interpolating the gaps between consecutive images, and creating and displaying the 3-D model. The 3-D IMOD reconstruction of the anode microstructure is shown in Figure 2-1, along with a single anode cross-section (2-D) image. Each anode image is of size 370 pixels (height) × 430 pixels (width).

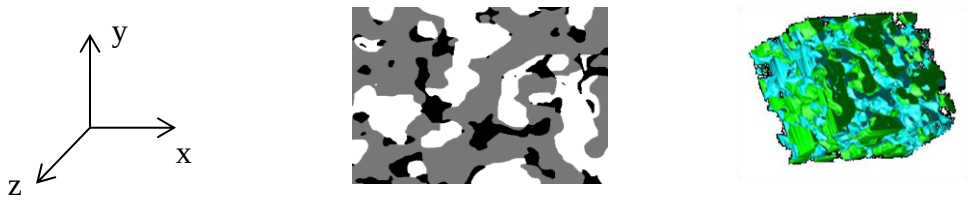


**Figure 2-1** (left) reference axes; (center) 2-D SEM image of anode microstructure cross-section [19]; (right) 3-D reconstruction of anode

In the SEM images of the anode, white (pixel value 255) corresponds to nickel, gray (pixel value 127) to YSZ, and black (pixel value 0) to the pores. The reconstructed 3-D IMOD model is used as a check on the geometry of the reconstructed 3-D FE model. The next step involves the creation of a single 2-D FE model from a single 2-D SEM image. This step is explained in detail in the following subsections.

*2.2.1. Image simplification schemes for finite element modeling*

The original anode image set used in this chapter consists of 82 images [19], while the original cathode image set (see Chapter 3) consists of 242 images [20]. Each anode image is of size 370 pixels (height) × 430 pixels (width), while each cathode image is of size 147 pixels (height) × 217 pixels (width). The original anode is of size 6.02 μm (x) × 5.18 μm (y) × 3.55 μm (z). The original cathode (see Chapter 3) is of size 8.85 μm (x) × 6.00 μm (y) × 12.85 μm (z). In the present study, 3-D finite element electrode microstructure models are reconstructed from a stack of 2-D microstructure images by assigning exactly one 3-D 8-node linear brick element to each volumetric pixel (i.e. voxel). The sizes of the 2-D images given above indicate that each 2-D image plane in the 3-D model would have around 160,000 elements in the anode and 32,000 elements in the cathode. Due to computational resource limitations, it is not possible to retain such a fine level of microstructural detail in the finite element models. To achieve computational efficiency, 41 images are used in the reconstruction of each 3-D model (anode and cathode) in Chapters 2 and 3. The original images of the electrode microstructures are also simplified to reduce the image resolution while retaining a sufficiently detailed microstructure for the purposes of

stress analysis. Detailed validation of an image simplification technique for achieving computational efficiency is provided in Chapter 3.

In this chapter, model simplification is achieved through image size reduction, which is implemented for the anode model by considering a subset of the original 2-D image pixel matrix. The subset is obtained by sampling pixels at regular intervals in the x- and y-directions, and is of size 74 rows × 86 columns. The original 2-D anode image pixel matrix is of size 370 rows × 430 columns. The x-y pixel resolution (14.0 nm) and the z-spacing between consecutive images (43.8 nm) are unchanged in the simplified model. Thus, the dimensions of each simplified anode image are 1.04 μm (height) × 1.20 μm (width), and the thickness (z-dimension) of the reconstructed model is 1.75 μm. These numbers indicate that the image size reduction scheme implemented in this chapter leads to a reduction in the reconstructed volume, which in turn may lead to a microstructure that is not entirely representative of the original anode.

A different image simplification scheme is implemented for the cathode model (see Chapter 3). This scheme, based on analyzing and simplifying consecutive (2 × 2) pixel squares in the image plane, preserves the overall x-y size of each image and the z-depth of the voxel, while leading to an increase in the x-y dimensions of each pixel. Due to the reduced number of images (41 images) used in reconstructing the cathode, the z-dimension of the cathode model (4.26 μm) is reduced compared to that of the original (12.85 μm). Thus the (2 × 2) simplification scheme also leads to a reduction in the reconstructed volume. However, as validated in detail in Chapter 3, the (2 × 2) scheme leads to a reasonably good approximation of the original microstructure.

Finally, in Chapter 4, a simplification scheme similar to the (2 × 2) scheme described above is used for both anode and cathode models. This scheme is based on $(n \times n)$ pixel square simplification, where $n$ = 10 for the anode and $n$ = 6 for the cathode. This level of simplification is necessary to achieve reasonable computational efficiency with cohesive elements, as explained in Chapter 4. The $(n \times n)$ simplification schemes again preserve the overall x-y dimensions of each image. As explained in Chapter 4, these

$(n \times n)$ schemes also ensure that the overall z-dimension of the model is equal to that of the original microstructure, at the expense of increasing the z-depth of the voxel due to the limited number of images used in the reconstruction. In Chapter 4, the plausibility of the ($n \times n$) schemes is demonstrated by showing that the schemes lead to values of standard microstructural parameters that are within acceptable ranges established in the experimental literature for both anode and cathode.

The above discussion reveals that each of the different simplification schemes has its own advantages and disadvantages. While the image size reduction scheme is easy to implement, it may not lead to a representative microstructure in the FE model. Although the $(n \times n)$ pixel square simplification schemes ($n$ = 2, 6, 10) are more complicated, they may lead to good approximations of the original microstructure. A detailed comparison and validation study of these approaches may be an interesting topic for future research.

*2.2.2. Finite element models*

The anode image set used in this chapter originally consists of 82 images [19], of which 41 are used for 3-D model reconstruction. The in-house algorithms and programs developed for generating image-based FE models are initially tested by creating a single image-based 2-D FE model. Modeling is carried out using the commercial FE software ABAQUS v6.9 [24]. This is done by writing a MATLAB ® program [25] to recreate the geometry of the image using 2-D finite elements (4-node quadrilateral elements) and to write the geometry data to an ABAQUS input file. Exactly one element is assigned to each pixel in the image, and the element is included in the appropriate element set (nickel or YSZ) based on the corresponding pixel value. Information concerning the material properties, boundary conditions, initial temperature, operating temperature field, and required outputs (e.g. principal stresses) is also specified in the input file. The input file is then analyzed using ABAQUS to generate the 2-D FE model shown in Figure 2-2.

**Figure 2-2** Two-dimensional FE model of a single cross-section of the SOFC anode

The 3-D FE anode models are generated by creating a stack of all the 2-D images and introducing a "buffer" plane between each pair of consecutive images. This is necessary and useful to ensure a simple step variation in material properties between corresponding regions in two consecutive images. The gaps between consecutive images and buffer planes are then interpolated by assigning one three-dimensional 8-node linear brick element to each voxel. Thus, the 3-D geometry of the anode microstructure is reconstructed in the 3-D FE model of the anode. The reconstructed 3-D FE anode model is shown in Figure 2-3, along with various free-body cuts.

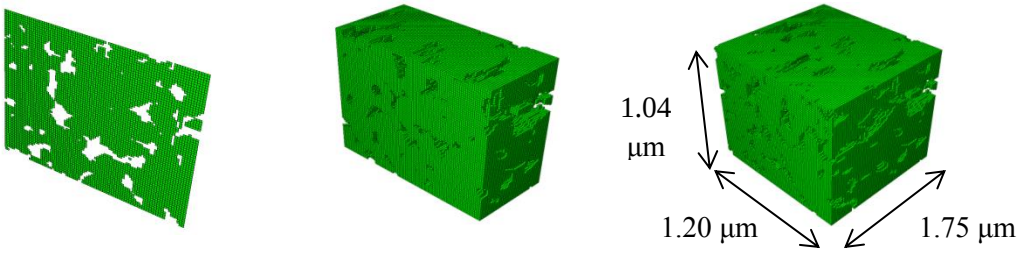


**Figure 2-3** Free-body cuts of the three-dimensional FE model of the SOFC anode

## 2.3. Finite element analysis of anode models

### *2.3.1. Analysis models and metrics*

Finite element analysis (FEA) of the anode models is carried out to investigate the effect of various thermal loads, as well as the effect of variation of material properties with temperature, on the mechanical integrity and probability of failure of the models. The effect of nonlinear (elastic-plastic) behavior versus

linear elastic behavior of nickel is also investigated, which has not been studied in detail in the literature. The FE analyses are divided into different categories as explained in Table 2-1. In each case, the FE model is subjected to fixed boundary conditions (i.e. all nodes on each of the six faces are allowed neither to translate nor to rotate). The behavior of the model with increasing thermal loads is investigated by subjecting the model to eight different spatially uniform temperature fields of magnitude $120^0$C, $220^0$C, $320^o$C, …, $820^0$C. In each steady-state analysis, the initial temperature is specified as $20^0$C (room temperature), so that the model is subjected to eight different magnitudes of temperature change ($\Delta T$ = $100^0$C, $200^0$C, $300^0$C, …, $800^0$C).

**Table 2-1** Metrics for finite element analyses of anode (CTE stands for coefficient of thermal expansion)

| Case | Ni | YSZ | Temperature-dependence (Ni) | Temperature-dependence (YSZ) |
|---|---|---|---|---|
| Case 1: Temperature-independent | Linear elastic | Linear elastic | None | None |
| Case 2: Temperature-dependent CTEs | Linear elastic | Linear elastic | CTE | CTE |
| Case 3: Elastic-plastic behavior of Ni | Elastic-plastic | Linear elastic | CTE | Young's modulus, CTE |

*2.3.2. Material properties*

Table 2-2 lists the room temperature material properties used for nickel and YSZ [3, 16]. Figure 2-4 shows the variation of the coefficients of thermal expansion of nickel and YSZ with temperature [16]. Figure 2-5 shows the variation of the Young's modulus of YSZ with temperature [12].

**Table 2-2** Room temperature material properties used in FE analyses of anode [3, 16]

| Material | Young's modulus (GPa) | Poisson's ratio | Coefficient of thermal expansion ($10^{-6}$ $^0C^{-1}$) |
|---|---|---|---|
| Nickel | 207 | 0.31 | 12.50 |
| YSZ | 205 | 0.30 | 10.40 |

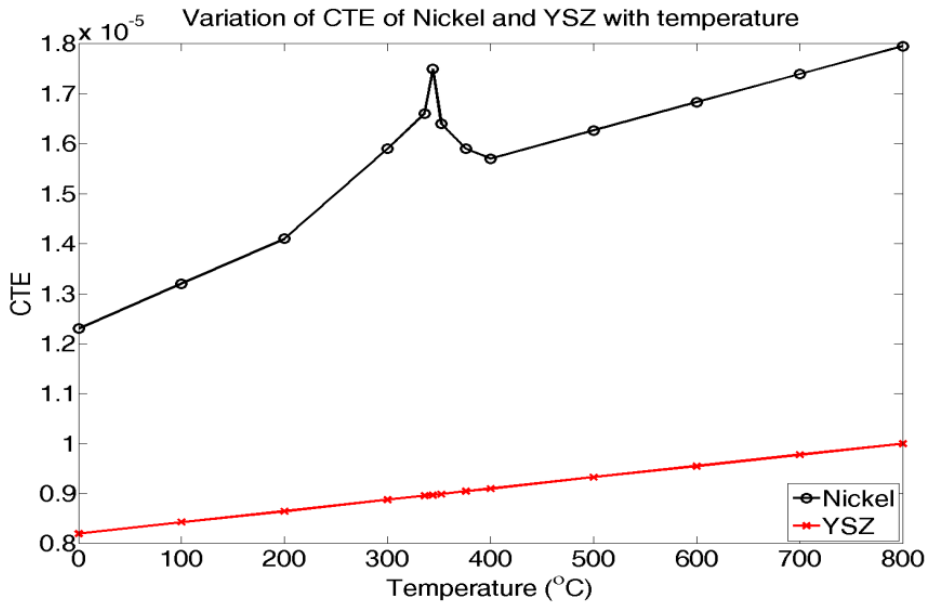


**Figure 2-4** Variation of CTE of nickel and YSZ with temperature [16]

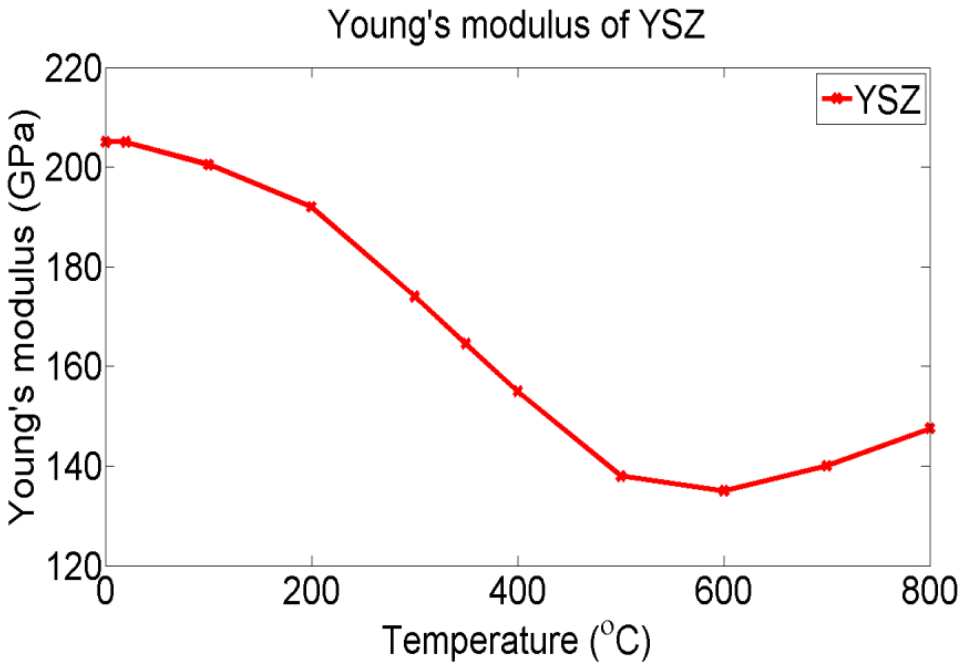


**Figure 2-5** Variation of Young's modulus of YSZ with temperature [12]

The Young's modulus of nickel is assumed to be constant over the temperature range considered. The room temperature value of the Young's modulus of nickel (as shown in Table 2-2) is used in the FE analyses of the anode. Figure 2-6 shows the stress-plastic strain curve used to describe the nonlinear

behavior of nickel [26]. It is assumed that the stress-strain curve of nickel does not change over the temperature range considered.

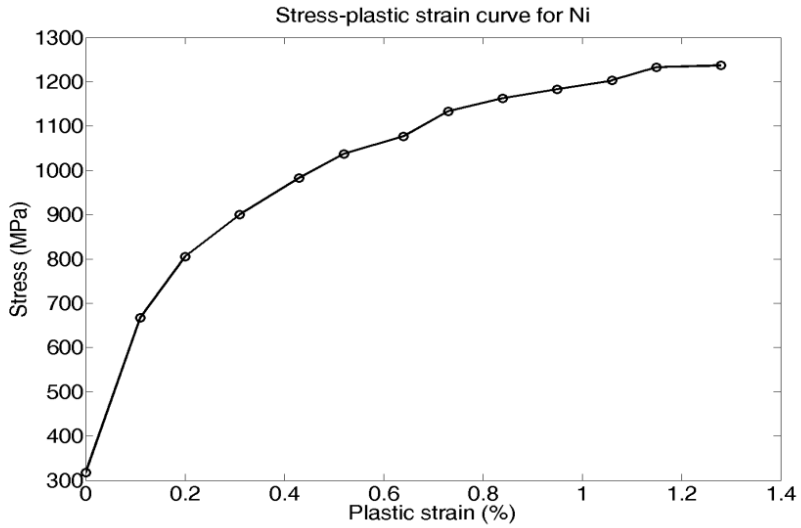


**Figure 2-6** Stress-plastic strain curve for nickel [26]

## 2.4. Results and discussion

### *2.4.1. Stress analysis*

The 3-D FE model of the anode (50:50 NiO:YSZ weight percentage (wt. %) composition) is shown in Figure 2-7. The model consists of 406,465 elements and 473,181 nodes.

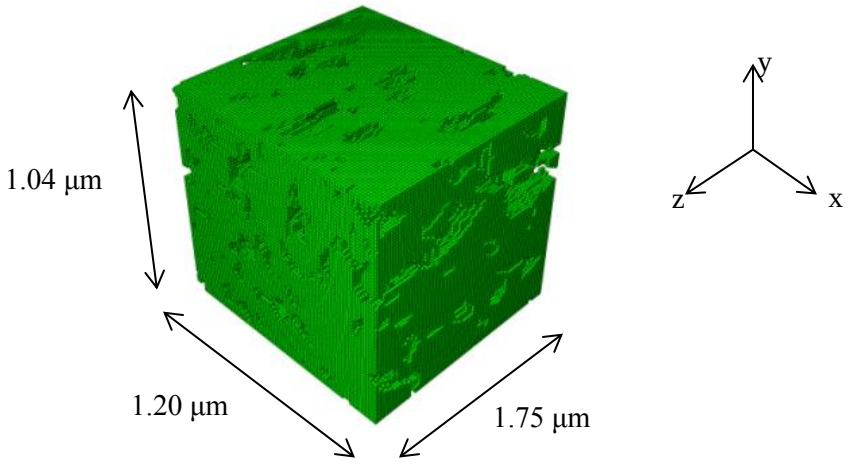


**Figure 2-7** Three-dimensional FE model of anode

The von Mises stress contours for the anode at $\Delta T = 100^0C$, $500^0C$, and $800^0C$ are shown considering elastic-plastic behavior of nickel in Figure 2-8. The stress values are in units of N $m^{-2}$ (i.e., Pa).

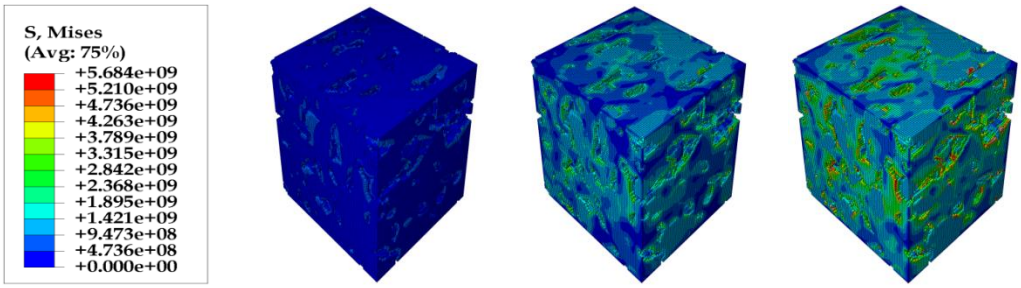


**Figure 2-8** Von Mises stress contour plots (in Pa) for anode considering elastic-plastic behavior of nickel: (left to right) $\Delta T = 100^0C$, $\Delta T = 500^0C$, $\Delta T = 800^0C$

Figure 2-8 shows that as $\Delta T$ increases from $100^0C$ to $800^0C$, the stresses in the anode also increase. This happens because thermal stress is proportional to the CTE, and the CTEs of both nickel and YSZ increase with temperature, as seen from Figure 2-4. Also, the stress plots show that the stresses are greater near the regions of pores due to stress concentration, as expected. Similar results are obtained for the cases with temperature-independent material properties and temperature-dependent CTEs. The effect of the elastic-plastic behavior of nickel on the principal tensile stress values (as compared with the linear elastic behavior assumed in the cases with temperature-independent material properties and temperature-dependent CTEs) is discussed in subsection 2.4.2, which deals with probability of failure calculations for the anode.

*2.4.2. Probability of failure analysis*

Ceramic materials exhibit brittle behavior under tensile stress. Also, unlike metals, they show wide variability in tensile strength values and follow a statistical strength distribution. Thus, the Weibull method of analysis [14, 21] is used to calculate the probability of failure of the SOFC anode. According to the Weibull method, the survival probability of a particular component $j$ under the action of a tensile stress $\sigma$ is given by [14]:

$$P_s^j\left(\sigma, V_j\right) = \exp\left( - \int_{V_j} \left( \frac{\sigma}{\sigma_0} \right)^m \frac{dV_j}{V_0} \right) \qquad (2\text{-}1)$$

Here, $j$ = anode, $V_j$ is the volume of component $j$, $V_0$ is a characteristic specimen volume (reference volume) for the material of component $j$, $\sigma_0$ is the characteristic strength of the material of component $j$, and $m$ is the Weibull modulus of the material. The characteristic strength $\sigma_0$ is also the scale parameter for the distribution, while the Weibull modulus $m$ is the shape parameter. The reference volume $V_0$ is related to the characteristic strength $\sigma_0$ of the material. In this study, the Weibull method is slightly modified to account for the fact that the anode is a composite made up of two different components, Ni and YSZ. The method employed is described next. The Weibull parameters used for the ceramic material (YSZ) are shown in Table 2-3 [14]. Only room temperature values of the Weibull parameters are used in this study.

**Table 2-3** Weibull parameters for anode ceramic material: room temperature values [14]

| Material | Weibull modulus, $m$ | Characteristic strength, $\sigma_0$ (MPa) | Reference volume, $V_0$ (mm$^3$) |
|---|---|---|---|
| YSZ | 7.0 | 446.0 | 0.35 |

The results of each stress analysis case are post-processed by writing programs to extract the three principal stress values from each YSZ element in the FE model. These principal stresses are then used to perform a Weibull analysis to determine the probability of failure of the anode at each ΔT value. Since the SOFC component materials are subjected to a multi-axial state of stress, the total survival probability of the ceramic phase of the anode under the action of the three principal stresses ($\sigma_1$, $\sigma_2$, and $\sigma_3$) is calculated. The principal stresses are assumed to act independently, and the total survival probability is calculated as the product of the survival probabilities under the action of each individual principal stress [14]:

$$P_s^j\left(\bar{\sigma}, V_j\right) = \prod_{i=1}^{3} P_s^j\left(\sigma_i, V_j\right) \qquad (2\text{-}2)$$

Also,

$$P_s^j\left(\sigma_i, V_j\right) = \exp\left(-\int_{V_j}\left(\frac{\sigma_i}{\sigma_0}\right)^m \frac{dV_j}{V_0}\right) \qquad (2\text{-}3)$$

Here, $j$ = YSZ for the anode, and $i$ = 1, 2, and 3. Only tensile values of the three principal stresses are used in the Weibull analysis. The probability of failure ($P_f$) of the YSZ phase is then calculated as follows [3]:

$$P_f = 1.0 - P_s^j\left(\bar{\sigma}, V_j\right) \qquad (2\text{-}4)$$

The probability of failure of the anode is calculated as the probability of failure of the YSZ phase, considering that the anode material (Ni-YSZ) is a metal-ceramic composite (cermet), and that the Weibull distribution is more appropriate for calculating the probability of failure of ceramics (such as YSZ) [14]. The strength distribution for metals (such as nickel) is closer to a normal distribution [27]. The probability of failure ($P_f$) value for the YSZ phase of the anode is calculated at each $\Delta$T value ($100^0$C, $200^0$C, …, $800^0$C) for each case described in Table 2-1. These values are plotted in Figure 2-9. Since these $P_f$ values are calculated on the basis of the tensile principal stresses in the YSZ phase, the variation of the maximum principal tensile stress (MPTS) in the YSZ phase of the anode with temperature in all three cases (temperature-independent material properties, temperature-dependent CTEs, and elastic-plastic behavior of Ni) is shown in Figure 2-10.

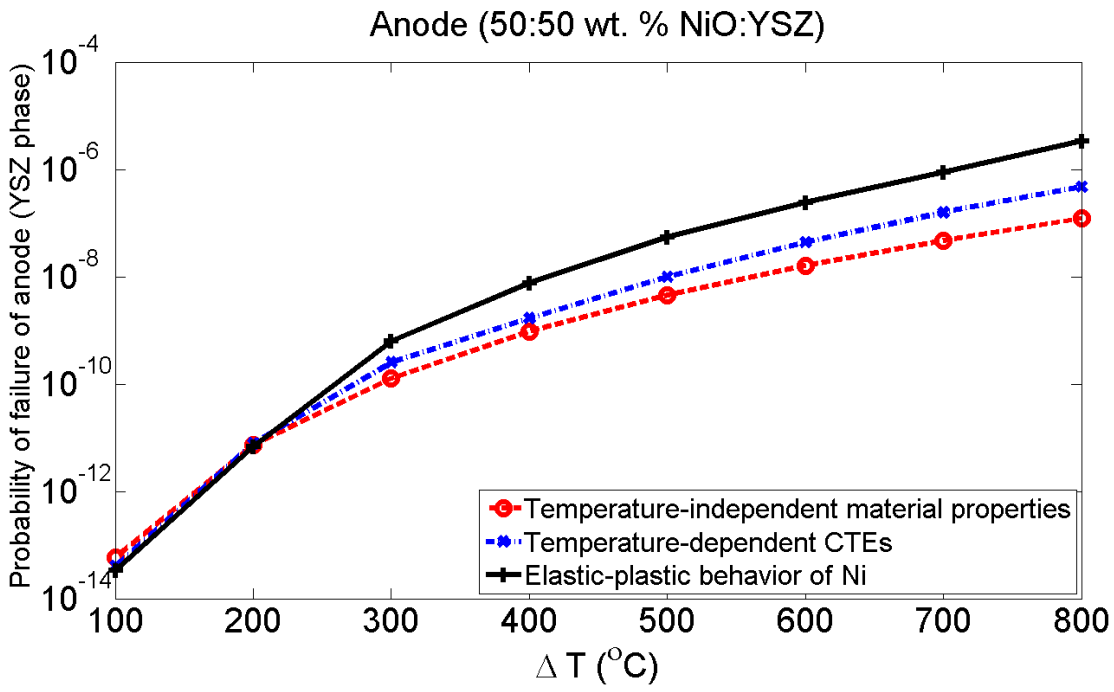


**Figure 2-9** Probability of failure of anode models

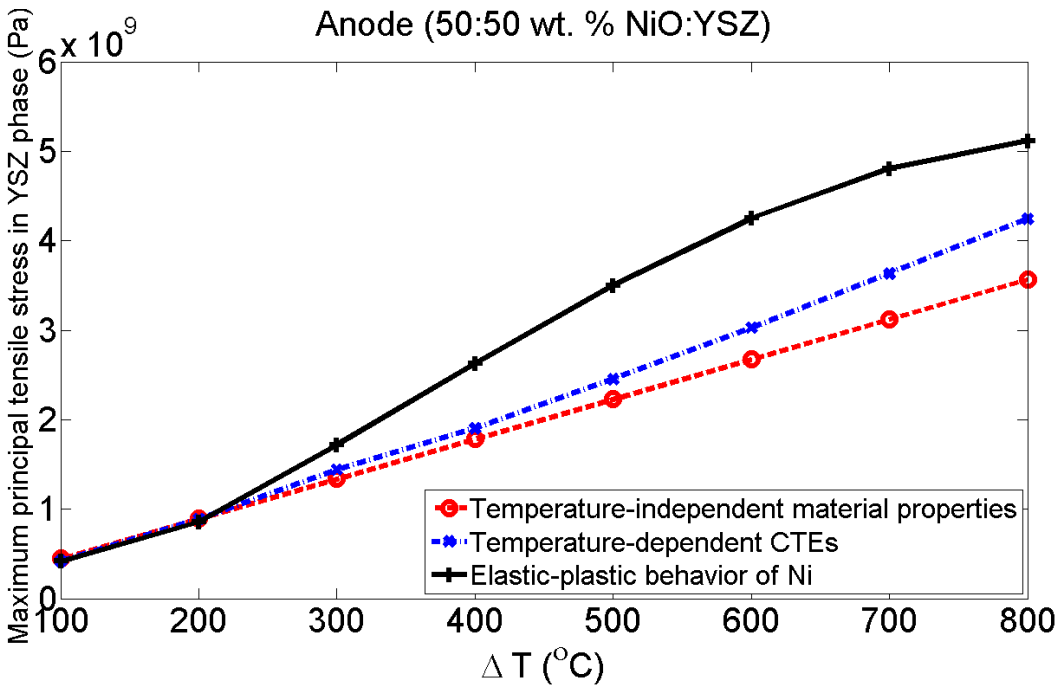


**Figure 2-10** Maximum principal tensile stress in the YSZ phase of the anode

The $P_f$ plot for the anode (Figure 2-9) shows that the probability of failure increases with increasing ΔT values (and hence increasing stresses), for each of the three cases considered (temperature-independent material properties, temperature-dependent CTEs, and elastic-plastic behavior of nickel). Also, the plot shows that the models with linear elastic material behavior significantly underestimate the probability of failure of the anode (defined by the $P_f$ values of the YSZ phase), as compared with the model that considers nonlinear elastic-plastic behavior of nickel, especially at high temperatures. This may be explained by referring to Figure 2-10, which shows that the maximum principal tensile stress (MPTS) in the YSZ phase of the anode increases with increasing ΔT values for all three cases. Figure 2-10 also shows that when the elastic-plastic behavior of Ni is taken into account, the MPTS in the YSZ phase attains higher values than when linear elastic behavior is assumed, especially at high temperatures. This can be explained as follows: when the Ni phase enters the nonlinear (plastic) part of its stress-strain curve at higher temperatures, lower stresses are induced in the Ni phase than if its stress-strain curve had been purely linear elastic with the same value of Young's modulus. Thus, when the Ni phase starts exhibiting nonlinear behavior, a higher proportion of the thermal stresses must be redistributed into the YSZ phase, resulting in higher MPTS values in the YSZ phase (and hence higher $P_f$ values for the anode).

Figure 2-9 also shows that the case with temperature-dependent CTEs shows higher $P_f$ values than the case with temperature-independent material properties at intermediate and high temperatures. Again, Figure 2-10 shows that with temperature-dependent CTE values, higher tensile stresses are induced in the YSZ phase of the anode than with temperature-independent material properties, especially at intermediate and high temperatures. This can be explained by referring to Figure 2-4, which shows that the CTEs of both Ni and YSZ increase with temperature. Since thermal stresses are proportional to CTE values, it can be expected that the case with temperature-dependent CTEs will show higher MPTS values (and hence higher $P_f$ values) than the case with temperature-independent material properties, which uses constant (room-temperature) values of the CTEs.

## 2.5. Conclusion

Three-dimensional FE models of SOFC anode microstructures are constructed from a stack of two-dimensional SEM images of actual cross-sections. The models are subjected to spatially uniform temperature fields of increasing magnitude and the resulting distribution of thermal stresses is obtained using FEA. The obtained stresses are subjected to Weibull analyses to determine the probability of failure of the anode microstructure as a function of temperature. The novelties of this work include FE analysis of thermal stresses induced in microstructure-based anode models under spatially uniform thermal loads, consideration of temperature-dependent material properties of the anode materials, and consideration of nonlinear elastic-plastic behavior of the nickel phase of the Ni-YSZ anode. The Weibull analyses show that the linear elastic material models underestimate the probability of failure of the anode at high temperatures; hence, it is important to consider the elastic-plastic behavior of the nickel phase of the Ni-YSZ anode. In this work, steady-state analysis has been performed. Residual stresses have not been considered in this study due to lack of such information, and simple, spatially uniform temperature fields have been used to model thermal loads.

# Chapter 3

## Finite Element Thermal Stress Analysis of SOFC Cathode Microstructures: Effects of Varying Phase Volume Fractions and Temperature-Dependent Material Properties

### 3.1. Introduction

In this chapter, finite element analysis (FEA) of thermal stresses induced in reconstructed SOFC cathode microstructures under spatially uniform temperature fields is performed. Three-dimensional finite element (FE) models of SOFC cathode microstructures are generated from a stack of two-dimensional microstructure images. The models are subjected to FEA to determine thermal stresses due to steady-state temperature change from room temperature up to operating temperature. The calculated thermal stresses are analyzed using the Weibull method to calculate the probability of failure. The cathode material is 50:50 wt. % LSM-YSZ. The effects of temperature-dependent material properties on the probability of failure of the cathode are investigated. A cathode model of 30:70 wt. % LSM:YSZ composition is derived using a heuristic scheme to investigate the effects of varying phase volume fractions on mechanical integrity and probability of failure under thermal loads.

This study extends the work described in Chapter 2 by including detailed validation of original and derived microstructures. The effects of varying phase volume fractions on the mechanics of cathode microstructures under thermal stress are considered. A simple heuristic scheme is developed to derive cathode microstructures of varying compositions within a limited range from the original, real microstructures. Construction of such derived microstructures provides physical insights into the effects of phase compositions on the mechanics of electrode structures in SOFCs, which in reality possess varied compositions through the thickness direction to increase material compatibility between electrolyte and electrodes and to improve overall cell performance.

### 3.2. Image-based finite element cathode microstructure models

*3.2.1. Models based on original images*

Three-dimensional (3-D) FE microstructure models are reconstructed from 41 two-dimensional (2-D) cross-sectional images of a cathode microstructure. The 2-D images have been obtained by Dr. Scott Barnett's research group at Northwestern University [20], using focused ion beam-scanning electron microscopy (FIB-SEM). Examples of the 2-D images are shown in Figure 3-1. These images are of the real cathode microstructure having 50:50 LSM:YSZ composition. The original cathode image set consists of 242 images [20].

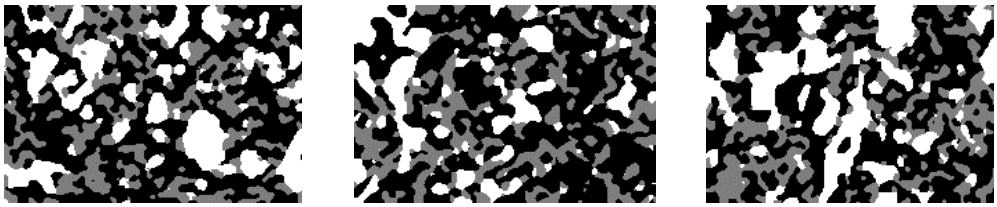

**Figure 3-1** Two-dimensional SEM images of cathode cross-sections [20]

In the SEM cathode images, white (pixel value = 255) represents LSM, gray (pixel value = 127) represents YSZ, and black (pixel value = 0) represents the pores. The original cathode image dimensions are 217 pixels (width) × 147 pixels (height).The in-plane, x-y spatial resolution between pixels is 40.8 nm and the z-spacing between images is 53.3 nm. The original cathode images are thus of size 8.85 μm (width) × 6.00 μm (height). Finite element modeling is carried out using the commercial FE software ABAQUS [24]. This is done by writing MATLAB ® [25] programs to generate ABAQUS input files with all relevant data for running the FE analysis: model geometry, material properties, boundary conditions, initial temperature, operating temperature field and required output data. The 3-D FE model is reconstructed from the images using 3-D finite elements (8-node linear brick elements). In order to increase computational efficiency for 3-D analysis using the finite element method, the full model is simplified to a representative model in which some details of phase geometry are sacrificed, but the microstructural skeleton that is crucial to stress analysis remains almost unchanged. To provide validation

data for this approach, 2-D cathode microstructure images are used for calculating three-phase boundary (TPB) density and phase surface area density for the original, full-size 50:50 wt. % LSM:YSZ cathode, as well as for the simplified 50:50 cathode. The data agree reasonably well with those reported in the literature [5, 20] (see Table 3-2 and Table 3-3). This quantitative evidence may support the validity of the simplified model within a limited range, which provides a basis for mechanical stress analysis that can achieve computational efficiency.

Based on reviewers' comments on a publication [28] resulting from this work, a simplification scheme that analyzes and simplifies consecutive (2 × 2) pixel squares in the image plane is implemented. A subset, of size 146 rows × 172 columns, of the original 2-D image pixel matrix is considered. For each such 2-D image subset, consecutive squares of (2 × 2) pixels in the x-y plane are analyzed, and the numbers of LSM, YSZ, and pore pixels in each such (2 × 2) pixel square are counted. The phase that has the maximum number of pixels in the square is assigned as the final phase of that square in the simplified image. For a tie between LSM and YSZ, or between YSZ and pores, the pixel is assigned a value of 127 (YSZ). For a tie between pores and LSM, the pixel is assigned a value of 255 (LSM). This simplification scheme is validated by the volume fraction, surface area density, and three-phase boundary density calculations reported in Tables 3-1 and 3-2. As there are only 3 phases, and consecutive (2 × 2) pixel squares of 4 pixels each are considered, a tie between all 3 phases is not possible. Each such (2 × 2) pixel square in the original image corresponds to one pixel in the simplified image. Thus, in the simplified image, the square pixels in the x-y plane have an edge length of 81.6 nm. The depth of the voxel in the z-direction is 53.3 nm. The simplified images are of size 86 pixels (width) × 73 pixels (height). The dimensions of each simplified cathode image are 7.02 μm (width) x 5.96 μm (height). The thickness (z-dimension) of the simplified cathode model is 4.26 μm, so that the reconstructed volume of the simplified cathode model is 178 $\mu m^3$. The scheme preserves the overall x-y size of each 2-D subset and the z-depth of the voxel, while leading to an increase in the x-y dimensions of each pixel. Due to the reduced number of images (41 images) used in reconstructing the cathode, the z-dimension of the cathode model (4.26

μm) is reduced compared to that of the original (12.85 μm). Thus the (2 × 2) simplification scheme leads to a reduction in the reconstructed volume. However, as validated here in detail, the (2 × 2) scheme leads to a reasonably good approximation of the original microstructure.

The next step in the model generation process is image stacking. A stack of all the 2-D (x-y plane) images is created in the z-direction by using a cell array data structure to arrange the images consecutively. An initially blank "buffer" plane (of the same size as each image) is then introduced between each pair of consecutive images. This is necessary to achieve a simple "step" variation in material properties between corresponding regions in two consecutive images. The gaps between consecutive images are filled by assigning one 8-node linear brick element to each voxel. Consider the $n^{th}$ and $(n+1)^{th}$ images, and the buffer plane between them. The voxel connecting a given pixel on the $n^{th}$ image with the corresponding pixel location on the buffer plane is assigned to the element set corresponding to the value of the pixel on the $n^{th}$ image. Similarly, the voxel connecting a given pixel on the $(n+1)^{th}$ image with the corresponding pixel location on the buffer plane is assigned to the element set corresponding to the value of the pixel on the $(n+1)^{th}$ image. Thus, the 3-D geometry of the cathode microstructure is reconstructed in the 3-D FE cathode model, with a step variation in material regions between consecutive images. The volume fractions of phases in each 3-D model are calculated by counting the number of voxels corresponding to each phase (based on pixel value), and dividing by the total number of voxels in the model (Table 3-1).

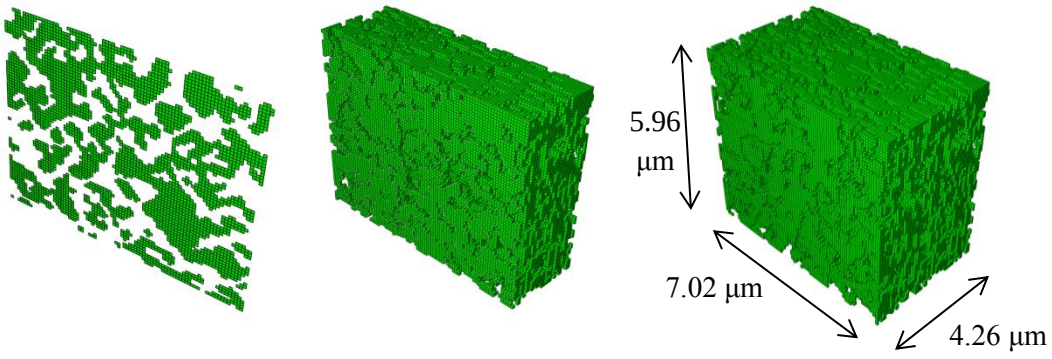


**Figure 3-2** Free-body cuts of the three-dimensional reduced-size FE cathode model (50:50 LSM:YSZ)

*3.2.2. Derived model and validation*

In order to study the effect of composition on the probability of failure of the cathode, a 3-D model having volume fractions different than those of the original 50:50 LSM:YSZ model is derived from the original images. The compositions of the models included in this study are given in Table 3-1 below.

**Table 3-1** Original (50:50) and derived (30:70) LSM:YSZ compositions of cathode [5]

| Model size and wt. % LSM:YSZ | $V_f$ LSM (%)$^A$ | $V_f$ LSM (%)$^L$ | $V_f$ YSZ (%)$^A$ | $V_f$ YSZ (%)$^L$ | $V_f$ Pores (%)$^A$ | $V_f$ Pores (%)$^L$ |
|---|---|---|---|---|---|---|
| Full, 50:50 | 22.93 | 22.94 | 24.62 | 25.29 | 52.45 | 51.77 |
| Simplified, 50:50 | 24.16 | 22.94 | 26.89 | 25.29 | 48.95 | 51.77 |
| Simplified, 30:70 | 16.24 | 14.12 | 39.83 | 36.80 | 43.93 | 49.08 |

$V_f$ = phase volume fraction, $^A$ = values from algorithm, $^L$ = values from literature [5]

A heuristic scheme is developed to derive the 3-D cathode model of 30:70 LSM:YSZ composition from the original 50:50 LSM:YSZ images. Boundary pixel modification is used to effect volume fraction alterations. This algorithm involves the identification of pixels initially lying on two- or three-phase boundaries in the original images, by comparison of pixel values with nearest in-plane neighbors. Boundary pixels are identified as black pixels at corresponding locations in a new, initially empty cell array (the "boundary array"), while interior pixels are identified as white pixels in this new boundary array, which is of identical size as the original image stack. The locations of boundary pixels in the original image array are picked out from the boundary array by identifying black pixels in it. The values of pixels adjacent to boundary locations in the original image array are modified according to heuristic rules derived by trial-and-error, until the desired volume fractions of each phase are obtained in the corresponding 3-D model. The boundary pixel identification algorithm is illustrated in Figure 3-3.

The steps in the heuristic algorithm are illustrated in Figure 3-4, which shows how the algorithm operates in a step-by-step manner on cathode images from the 50:50 model to derive the 30:70 model by changing the relative proportions of pixels of different phases. The microstructural characteristics of the derived

30:70 cathode model are validated by calculating three-phase boundary (TPB) density and phase surface area densities from the stack of 2-D images, and comparing these values with data available in the literature (Tables 3-2 and 3-3). The TPB density and surface area density calculation algorithms are first validated by calculating the TPB and surface area densities for the full-size 50:50 cathode model, for which data are already available in the literature [5, 20]. TPB length is calculated from the 2-D image stack using the boundary array described above, by identifying three-phase boundary points through pixel value comparison with nearest neighbors. TPB density ($\mu m^{-2}$) is calculated by dividing the TPB length ($\mu m$) by the total reconstructed volume of the corresponding model ($\mu m^3$).

The phase surface area is calculated from the boundary array by counting the total number of surface elements belonging to each phase. Finally, the surface area density ($\mu m^{-1}$) of that phase is calculated by dividing the total surface area of the phase ($\mu m^2$) by the total reconstructed volume of the model ($\mu m^3$).

**Table 3-2** Full and simplified cathode models, LSM-YSZ [5, 20]

| Model (wt. %) | TPB density$^A$ ($\mu m^{-2}$) | TPB density$^L$ ($\mu m^{-2}$) | LSM SA density$^A$ ($\mu m^{-1}$) | LSM SA density$^L$ ($\mu m^{-1}$) | YSZ SA density$^A$ ($\mu m^{-1}$) | YSZ SA density$^L$ ($\mu m^{-1}$) | Pore SA density$^A$ ($\mu m^{-1}$) | Pore SA density$^L$ ($\mu m^{-1}$) |
|---|---|---|---|---|---|---|---|---|
| Full (50:50) | 5.74 | 7.35 | 1.83 | 1.80 | 3.08 | 3.00 | 4.05 | 3.90 |
| Simplified (50:50) | 4.94 | 7.35 | 1.29 | 1.80 | 2.07 | 3.00 | 2.89 | 3.90 |
| Simplified (30:70) | 7.48 | 6-9 | 1.15 | 1.30 | 2.86 | 4.39 | 2.82 | 4.70 |

SA = surface area, $^A$ = values from algorithm, $^L$ = values from literature [5, 20]

**Table 3-3** Volumes of full and simplified cathode models

| Model | X-Y pixel resolution (nm) | Z-spacing between images (nm) | Height (pixels/$\mu m$) | Width (pixels/$\mu m$) | Number of images used | Volume of model ($\mu m^3$) |
|---|---|---|---|---|---|---|
| Full | 40.8 | 53.3 | 147 / 6.00 | 217 / 8.85 | 242 | 682 |
| Simplified | 81.6 | 53.3 | 73 / 5.96 | 86 / 7.02 | 41 | 178 |

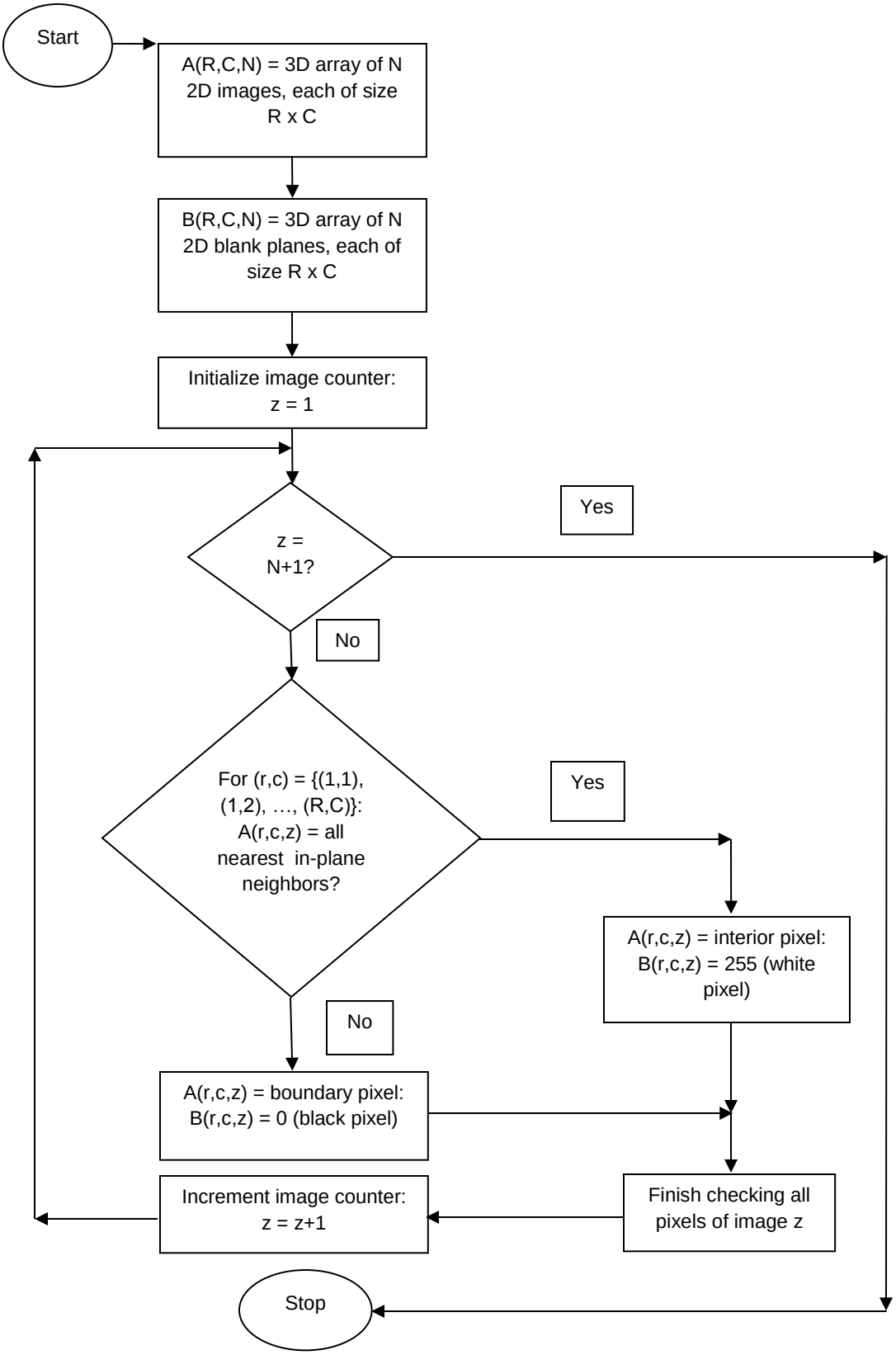


**Figure 3-3** Algorithm for boundary pixel detection

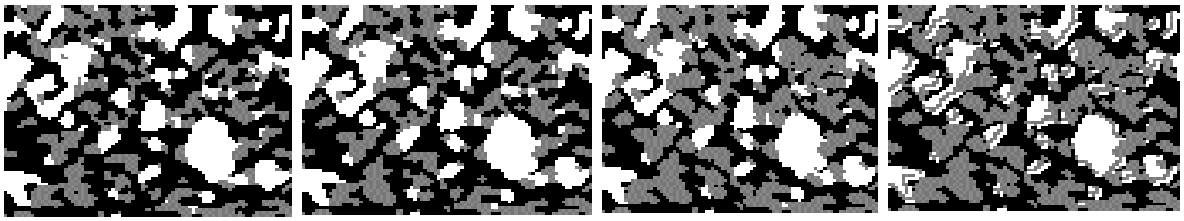

Cathode 5050 1st step 2nd step 3rd step (Cathode 3070)

**Figure 3-4** Boundary pixel modification heuristic scheme

From Table 3-2, we can see that the TPB and surface area densities calculated by the algorithms for the full and reduced 50:50 cathode models agree reasonably well with those reported in the literature. There is similar agreement between calculated and reported surface area and TPB densities for the reduced 30:70 cathode model derived from the original images. The differences are probably due to the fact that the TPB density calculation algorithm makes use of the 2-D images, while the values reported in [5] are based on detailed analysis of the 3-D microstructure data set and on an analytical model [29]. It is worth noting here that Vivet et al. [30] have reported TPB densities as high as 7.2 – 11.2 $\mu m^{-2}$ for Ni-YSZ anode cermet samples having NiO wt.% values varying from 45% to 61%, with sample volumes varying from 349.39 to 957.95 $\mu m^3$. Moreover, Wilson et al. [5] have pointed out that TPB density may be higher for cathodes than for anodes due to the finer cathode microstructures. Considering these data, the TPB and surface area densities calculated for the simplified 50:50 and 30:70 cathode models may be considered reasonable, given that the reconstructed volume for the simplified cathode is approximately 178 $\mu m^3$ (Table 3-3).

### 3.3. Finite element thermal stress analysis

#### *3.3.1. Study design*

Finite element analyses of the cathode microstructure models are carried out to investigate thermal stresses due to various temperature fields. The effects of varying phase volume fractions and temperature-dependent material properties on thermal stresses and probability of failure are investigated. The FE

analyses are divided into different categories as explained in Table 3-4. In each case, the FE model is subjected to fixed boundary conditions (i.e. all nodes on each of the six faces are allowed neither to translate nor to rotate). The behavior of the model with increasing thermal loads is investigated by subjecting the model to eight different spatially uniform temperature fields of magnitude $120^0$C, $220^0$C, $320^0$C, …, $820^0$C. In each analysis, the initial temperature is specified as $20^0$C (room temperature), so that the model is subjected to eight different magnitudes of temperature change ($\Delta T = 100^0$C, $200^0$C, $300^0$C, …, $800^0$C).

**Table 3-4** Finite element analyses of cathode

| Case | LSM | YSZ | Temperature-dependence (LSM) | Temperature-dependence (YSZ) |
|---|---|---|---|---|
| Temperature-independent | Linear elastic | Linear elastic | None | None |
| Temperature-dependent | Linear elastic | Linear elastic | Young's modulus | Young's modulus, CTE |

*3.3.2. Material Properties*

Table 3-5 lists the room temperature material properties used for YSZ and LSM [3].

**Table 3-5** Room temperature material properties used in FE analyses of cathode [3]

| Material | Young's modulus (GPa) | Poisson's ratio | CTE ($10^{-6}\ ^0C^{-1}$) |
|---|---|---|---|
| YSZ | 205 | 0.30 | 10.40 |
| LSM | 40 | 0.25 | 11.40 |

Figure 3-5 shows the variation of the CTE of YSZ with temperature [16] and the variation of the Young's modulus of LSM and YSZ with temperature [12]. The CTE of LSM is assumed constant over the temperature range considered. The room temperature value of the CTE of LSM (Table 3-5) is used in the FE analyses.

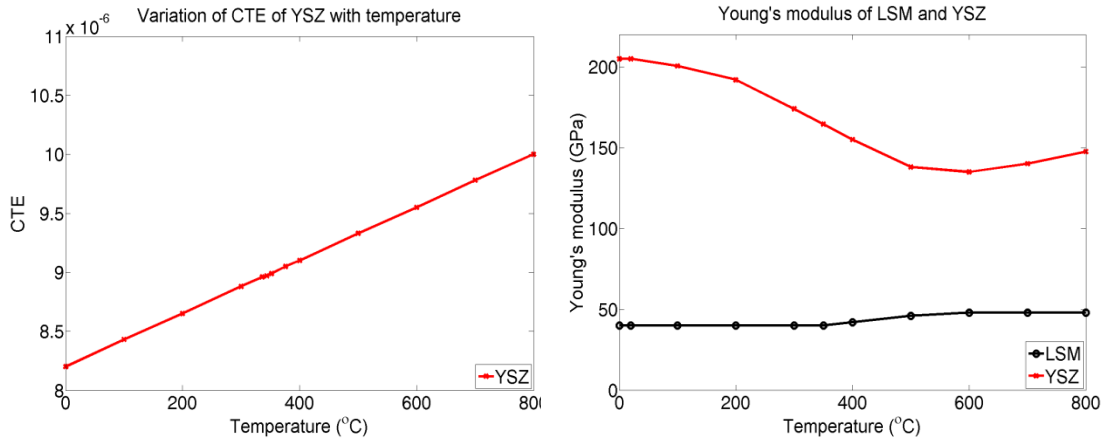


**Figure 3-5** (left) Variation of CTE of YSZ with temperature [16]; (right) variation of Young's modulus of LSM and YSZ with temperature [12]

*3.3.3. Stress analysis*

The 3-D FE models of the cathode are shown in Figure 3-6. The models have approximately 260,000 elements and 400,000 nodes. Von Mises stress contour plots for the 50:50 wt. % LSM:YSZ cathode are shown, considering temperature-dependent material properties, in Figure 3-7. The stress values are in units of N $mm^{-2}$, i.e. MPa.

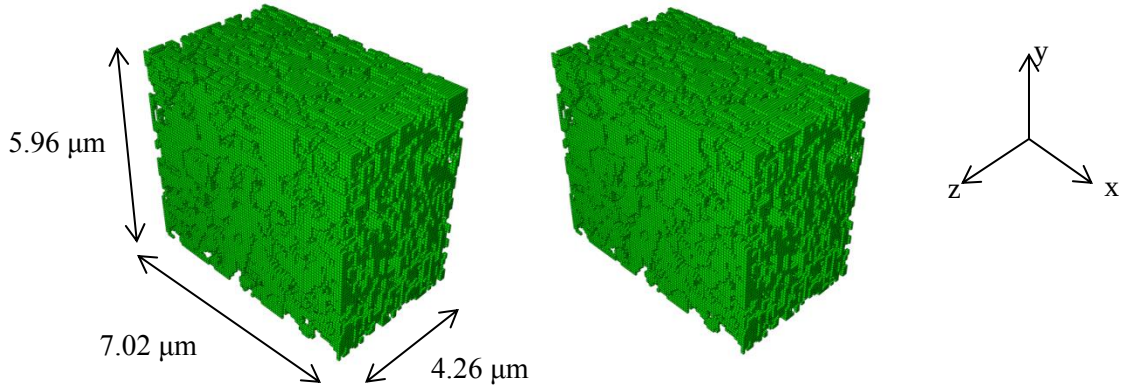


**Figure 3-6** Three-dimensional simplified FE models of 50:50 (left) and 30:70 (right) wt.% LSM:YSZ cathode

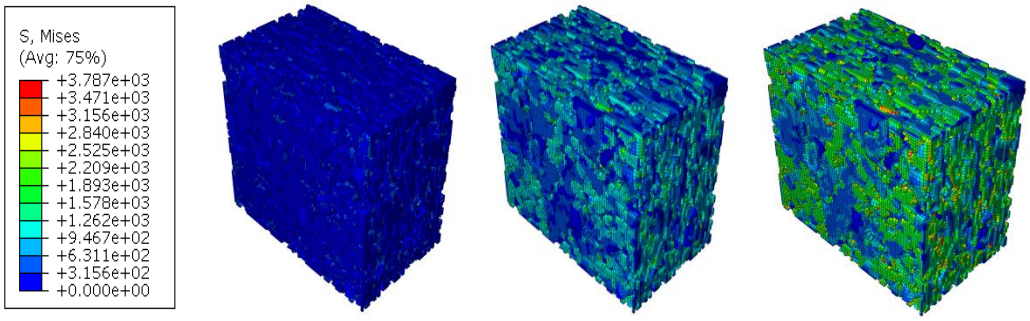


**Figure 3-7** Von Mises stress contour plots (in MPa) for 50:50 LSM:YSZ cathode considering temperature-dependent material properties: $\Delta T = 100^0C$ (left), $\Delta T = 500^0C$ (middle), $\Delta T = 800^0C$ (right)

Figure 3-7 shows that as $\Delta T$ increases from $100^0C$ to $800^0C$, the stresses in the cathode also increase. Thermal stress is proportional to the CTE and $\Delta T$, and the CTE of YSZ increases with temperature while the CTE of LSM is assumed constant over the temperature range considered. Also, the stress contours show that the stresses are greater near the pores due to stress concentration. Similar results are obtained for the case with temperature-independent material properties. The cathode model with 30:70 LSM:YSZ composition shows similar behavior in both cases. The effects of temperature-independent versus temperature-dependent material properties on the principal tensile stresses induced in the cathode are discussed in conjunction with probability of failure estimation, where the effects of varying phase compositions on thermal stresses and probability of failure are also discussed.

### 3.4. Estimation of probability of failure using the Weibull method

Ceramic materials exhibit brittle behavior under tensile stress. Also, unlike metals, they show wide variability in tensile strength values and follow a statistical strength distribution. Thus, the Weibull method of analysis [14, 21] is used to calculate the probability of failure of the SOFC cathode. According to the Weibull method, the survival probability of a particular component *j* under the action of a tensile stress $\sigma$ is given by [14]:

$$P_s^j(\sigma, V_j) = \exp\left( - \int_{V_j} \left( \frac{\sigma}{\sigma_0} \right)^m \frac{dV_j}{V_0} \right) \qquad (3\text{-}1)$$

Here $j$ = cathode, $V_j$ is the volume of component $j$, $V_0$ is a characteristic specimen volume (reference volume) for the material of component $j$, $\sigma_0$ is the characteristic strength of the material of component $j$, and $m$ is the Weibull modulus of the material. The characteristic strength $\sigma_0$ is also the scale parameter for the distribution, while the Weibull modulus $m$ is the shape parameter. The reference volume $V_0$ is related to the characteristic strength $\sigma_0$ of the material. In this study, the Weibull method is modified to account for the fact that the cathode material is a composite made up of two different components (LSM and YSZ). The Weibull parameters used for the ceramic materials (LSM and YSZ) are shown in Table 3-6 [14]. Room temperature values of the Weibull parameters are used in this study.

**Table 3-6** Weibull parameters for cathode ceramic materials: room temperature values [14]

| Material | Weibull modulus, $m$ | Characteristic strength, $\sigma_0$ (MPa) | Reference volume, $V_0$ ($mm^3$) |
|---|---|---|---|
| LSM | 7.0 | 52.0 | 1.21 |
| YSZ | 7.0 | 446.0 | 0.35 |

The results of each stress analysis case are post-processed by writing programs to extract the three principal stress values from each ceramic element (LSM or YSZ) in the cathode models. These principal stresses are then used to perform a Weibull analysis to determine the probability of failure of the cathode at each ΔT value. Since the SOFC component materials are subjected to a multi-axial state of stress, the total survival probability of each ceramic phase of the cathode under the action of the three principal stresses ($\sigma_1$, $\sigma_2$, and $\sigma_3$) is calculated. The principal stresses are assumed to act independently, and the total survival probability is calculated as the product of the survival probabilities under the action of each individual principal stress [14]:

$$P_s^j\left(\bar{\sigma}, V_j\right) = \prod_{i=1}^{3} P_s^j\left(\sigma_i, V_j\right) \qquad (3\text{-}2)$$

Also,

$$P_s^j\left(\sigma_i, V_j\right) = \exp\left[ -\int_{V_j} \left( \frac{\sigma_i}{\sigma_0} \right)^m \frac{dV_j}{V_0} \right] \qquad (3\text{-}3)$$

Here, $j$ = LSM or YSZ for the cathode, and $i$ = 1, 2, and 3. Only tensile values of the three principal stresses are used in the Weibull analysis. The probability of failure of each phase is then calculated as follows [3]:

$$P_f = 1.0 - P_s^j\left(\bar{\sigma}, V_j\right) \qquad (3\text{-}4)$$

*3.4.1. Probability of failure analyses*

Since the cathode is composed of two different ceramic materials (LSM-YSZ), the probability of failure of the cathode is calculated by extracting positive (tensile) values of the three principal stresses from each element in the LSM and YSZ element sets of the cathode FE model, and subjecting these to Weibull analyses. This results in two different probability of failure values (one each for the LSM and YSZ phases of the cathode), which are combined into a single probability of failure value for the cathode by assuming that the cathode fails when either phase fails or when both phases fail simultaneously. The probability that both phases fail simultaneously is calculated by assuming that the failures of the two phases are independent events, and hence the probability of simultaneous failure of the two phases is the product of the probabilities of failure of LSM and YSZ:

$$P_f(cathode) = P_f(LSMorYSZ) = P_f(LSM \cup YSZ)$$

$$\Rightarrow P_f(cathode) = P_f(LSM) + P_f(YSZ) - P_f(LSM \cap YSZ)$$

$$\Rightarrow P_f(cathode) = P_f(LSM) + P_f(YSZ) - P_f(LSM)\,P_f(YSZ)$$

The probability of failure ($P_f$) values for the LSM and YSZ phases of each cathode model are calculated and combined, as described above, at each ΔT value ($100^0$C, $200^0$C, …, $800^0$C) for both the cases described in Table 3-4 (temperature-independent material properties and temperature-dependent material properties). These values are plotted in Figure 3-8.

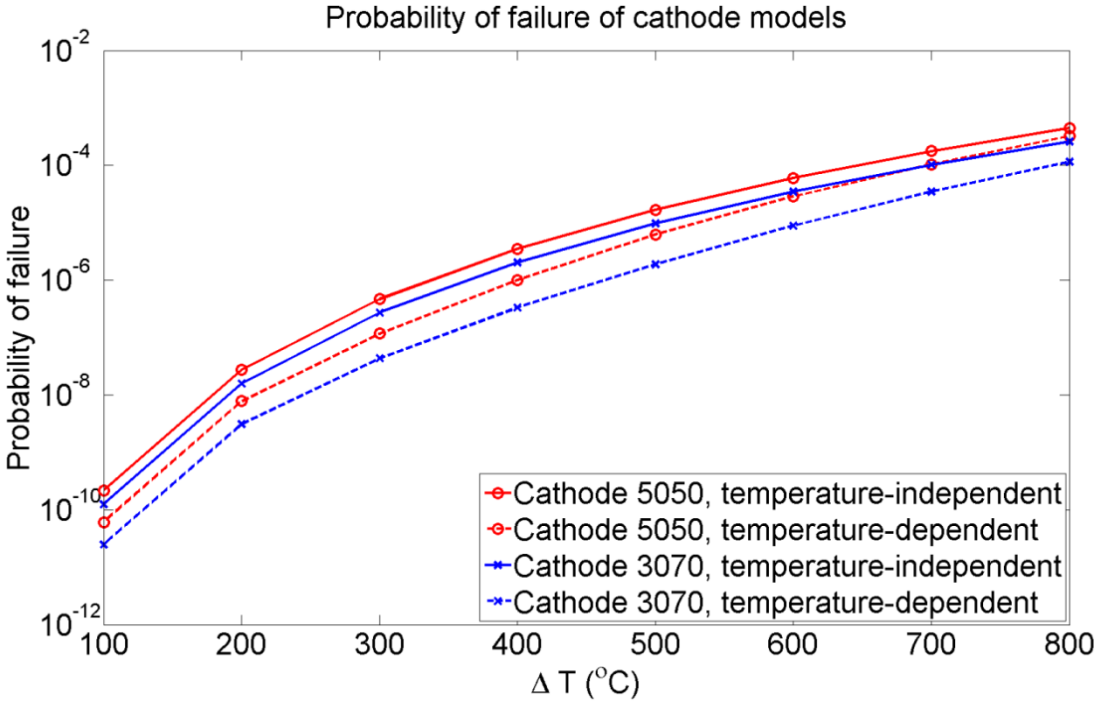


**Figure 3-8** Probability of failure of cathode models

The $P_f$ plots for both cathode models show that the probability of failure of the cathode increases with increasing ΔT values (and hence increasing stresses), for both temperature-independent and temperature-dependent material properties, as expected. These values may be verified against the cathode $P_f$ values reported by Anandakumar et al. [3]. They have investigated the probability of failure of functionally graded SOFCs subjected to spatially uniform thermal loading. Although the microstructures of the SOFC electrodes have not been considered in [3], the $P_f$ values reported in that work have been calculated using

the Weibull method, with the same Weibull parameter values as used in the present study. Anandakumar et al. [3] have reported (cf. Figure 16 in their paper) $P_f$ values varying in average from $10^{-12}$ to $10^{-5}$ for graded and layered LSM cathodes. The cathode $P_f$ values in the present study vary between $2.5 \times 10^{-11}$ and $4.5 \times 10^{-4}$, which is in good agreement with those reported in [3].

*3.4.1.1. Effects of temperature-dependent material properties*

As seen from Figure 3-8, higher $P_f$ values are obtained when temperature-independent material properties (indicated by the solid lines) are considered, for both cathode models. A physical explanation for this observation is suggested by the temperature variation of the Young's modulus of YSZ. For YSZ, E decreases from a value of 205 GPa at T = $20^0$C to a value of 147.5 GPa at $800^0$C, as shown in Figure 3-5. On the other hand, when temperature-independent material properties are considered, the Young's modulus of YSZ has a constant value of 205 GPa. This large decrease in the Young's modulus of YSZ with increasing temperature leads to lower stresses in the cathode with temperature-dependent material properties than with temperature-independent material properties. This in turn leads to lower $P_f$ values with temperature-dependent material properties than with temperature-independent material properties. This is confirmed by the MPTS plot for the 50:50 cathode model shown in Figure 3-9, which compares the maximum principal tensile stress induced in the YSZ and LSM phases of the model for temperature-independent and temperature-dependent material properties.

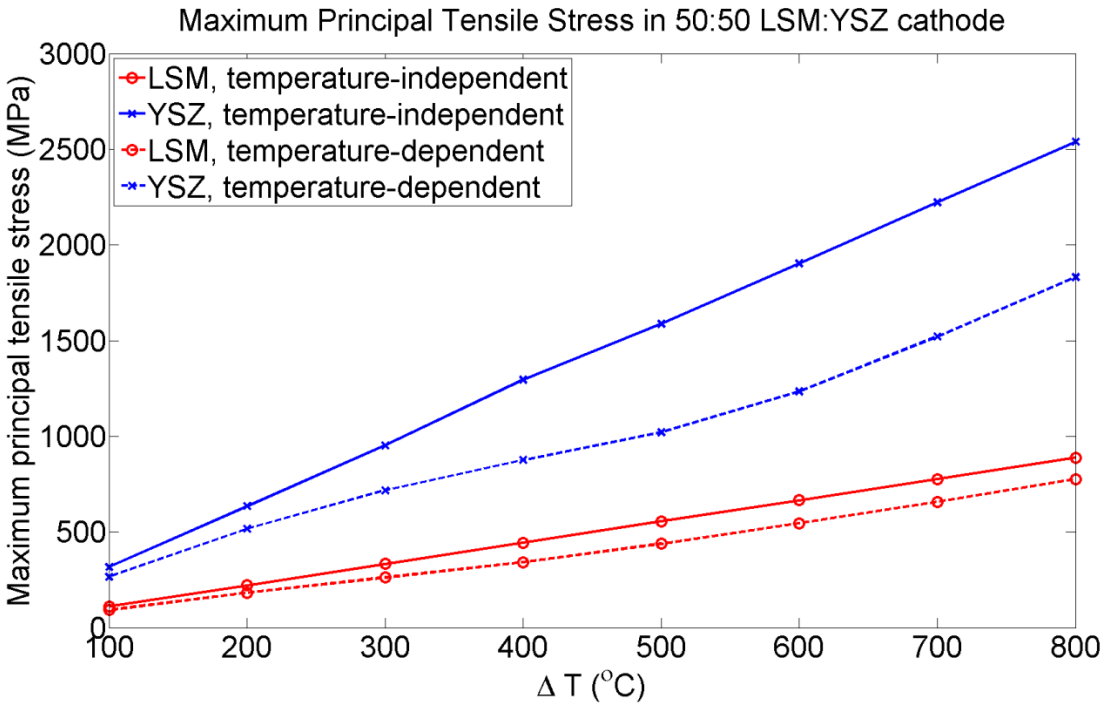


**Figure 3-9** Maximum principal tensile stress in LSM and YSZ phases of 50:50 LSM:YSZ cathode model

Figure 3-9 shows that the MPTS induced in the LSM phase for temperature-dependent material properties is lower than the MPTS induced in the LSM phase for temperature-independent material properties over the entire temperature range. Similarly, the MPTS induced in the YSZ phase for temperature-dependent material properties is lower than the MPTS induced in the YSZ phase for temperature-independent material properties over the entire temperature range. This implies that the cathode $P_f$ values, which are calculated on the basis of the tensile principal stresses in the LSM and YSZ phases, will be lower with temperature-dependent material properties than with temperature-independent material properties.

*3.4.1.2. Effects of variation of phase volume fractions*

Figure 3-8 shows the $P_f$ values for the two cathode models for temperature-independent and temperature-dependent material properties. For temperature-independent material properties, the 30:70 LSM:YSZ cathode model exhibits lower $P_f$ values than the 50:50 LSM:YSZ model over the entire temperature range. This may be due to greater stress concentration effects in the 50:50 LSM:YSZ cathode model,

given its higher pore volume fraction (48.95%) compared with the 30:70 LSM:YSZ cathode model (43.93%). Figure 3-8 also shows that when temperature-dependent material properties are considered, the volume fraction of YSZ plays a significant role in determining the $P_f$ values, since the Young's modulus of YSZ undergoes a large decrease with increasing temperature. Based on the previous discussion, we may anticipate that lower stresses will be induced in the 30:70 model, since it has a higher volume fraction of YSZ than the 50:50 model. These results are indeed observed in Figure 3-8. The 30:70 LSM:YSZ model shows lower $P_f$ values than the 50:50 model, for temperature-dependent material properties, in Figure 3-8.

### 3.5. Conclusion

This chapter addresses finite element thermal stress analysis of microstructure-based SOFC cathode models. It investigates the effects of temperature-dependent material properties and varying phase volume fractions of cathode materials on the behavior of the cathode microstructure model under thermal loads. In this chapter, an approximate heuristic volume fraction modification scheme is developed, based on boundary pixel modification of original 50:50 wt. % LSM:YSZ microstructure images. The scheme is used to derive a cathode microstructure of 30:70 wt. % LSM:YSZ composition. Construction of derived microstructures using such heuristic schemes may provide a simplified, approximate approach for investigating the effects of phase compositions on the mechanics of electrode structures, and is not intended to replace more rigorous approaches such as the random packing model. The critical findings are summarized as follows. First, consideration of temperature-independent material properties of the SOFC cathode materials results in higher probability of failure values than those obtained with temperature-dependent material properties. Second, with both temperature-independent and temperature-dependent material properties, the 30:70 LSM:YSZ cathode model is found to have lower probability of failure. For temperature-independent material properties, this is probably due to the lower pore volume fraction (i.e. lower stress concentration effects) in the 30:70 model. For temperature-dependent material properties, this is due to the decrease in the Young's modulus of YSZ with increasing temperature. The cathode probability of failure ($P_f$) values in the present study vary between $2.5 \times 10^{-11}$ and $4.5 \times 10^{-4}$, which is in

good agreement with those reported in [3] varying in average from $10^{-12}$ to $10^{-5}$ for graded and layered LSM cathodes. The present work does not consider the effects of residual stresses, which can be an interesting topic for future work.

# Chapter 4

# Finite Element Thermal Fatigue Analysis of SOFC Electrode Microstructures: Effects of Progressive Interface Degradation under Repeated Thermal Loading

## 4.1. Introduction

In this chapter, the effect of interface degradation under repeated thermal loading on the mechanical integrity and electrochemical performance of SOFC electrodes is studied through finite element simulations. Image-based 3-D models similar to those described in Chapters 2 and 3 are used in this study, with additional interface zones at the boundaries between dissimilar solid phases. These interface zones are composed of 3-D cohesive elements of small thickness. The effect of interface degradation on mechanical integrity is studied by subjecting 50:50 LSM:YSZ wt. % cathode models to increasing levels of thermal load from room temperature (20 $^0$C) up to operating temperature (820 $^0$C). Energy quantities (e.g. strain energy and damage dissipation) for cathode models with and without cohesive interface zones are obtained through FEA. These quantities are compared using energy balance concepts from fracture mechanics to gain insight into the effects of interface degradation on mechanical integrity.

The electrochemical performance of SOFCs is significantly influenced by three-phase boundary (TPB) zones in the microstructure. TPB zones are locations where all three phases comprising the microstructure - the two solid phases and the pore phase - are present. Electrochemical reactions such as oxygen reduction occur near TPBs, and TPB density is believed to affect the polarization resistance of the cathode [5, 20]. In this phase of the study, it is hypothesized that degradation of weak interfaces under thermal cycling has an adverse effect on TPB zones in the microstructure of the SOFC, leading to a reduction in electrochemical performance over time. Anode (50:50 NiO:YSZ wt. %) and cathode (50:50 LSM:YSZ wt. %) models are used in this part of the study. Interface degradation under thermal cycling is implemented in the FE electrode models through a simplified scheme. The scheme consists of five successive monotonic, steady-state heating operations from room temperature (20 $^0$C) up to operating temperature (820 $^0$C), combined with interface strength and fracture energy degradation in each heating

operation. Each thermal loading operation represents the heating phase of a normalized thermal cycle, where one normalized cycle represents 1000 actual thermal cycles. SOFCs have been known to perform with great reliability, showing no reduction in performance, for more than two years at a stretch [1]. Thus, it may be reasonable to assume that one normalized heating cycle in this study represents 1000 actual thermal cycles in the operating life of the cell. The interface degradation scheme is explained in detail later in this chapter.

### 4.2. Cohesive zone model

An interface damage initiation and evolution model is implemented in the three-dimensional (3-D) finite element (FE) SOFC electrode microstructures. The thin interface zones between dissimilar solid phases consist of 3-D cohesive elements available in ABAQUS v6.11 [31]. The 3-D cohesive elements, which are of negligible thickness compared with the neighboring solid elements, are used to simulate debonding between different solid phases at their interface. The 3-D cohesive elements are inserted between 8-node 3-D linear brick elements belonging to dissimilar solid phases, as shown below in Figure 4-1. Based on the in-plane (x-y) dimensions of the solid elements in the anode (14.0 nm) and cathode (40.8 nm), the thickness of the thin interface cohesive elements is chosen as 1 nm. Interfacial (fracture) energy is used as a reference value for bond strength between Ni and YSZ (anode), and between LSM and YSZ (cathode). Perfect bonding is assumed between elements belonging to the same solid phase. An algorithm based on the boundary pixel identification scheme (see Figure 3-3) is used to identify elements lying on solid phase boundaries.

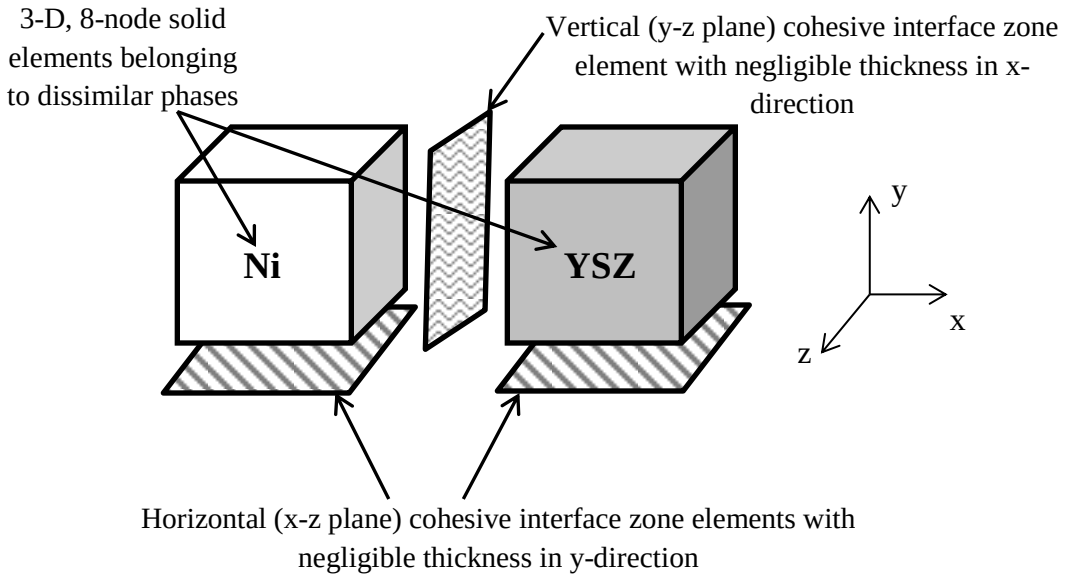


**Figure 4-1** Cohesive elements in the interface zone between solid elements of different phases

*4.2.1. Traction-separation behavior of cohesive elements*

The behavior of the interface cohesive zone elements is described using a traction-separation relation. Such a cohesive zone model (CZM) describes local material separation behavior by relating tractions (***t***) on the interface surfaces to material separation (***δ***). The CZM simulates progressive damage in the cohesive zone. The CZM, which is used to model imperfect bonding in highly porous electrodes of SOFCs, is illustrated in Figure 4-2.

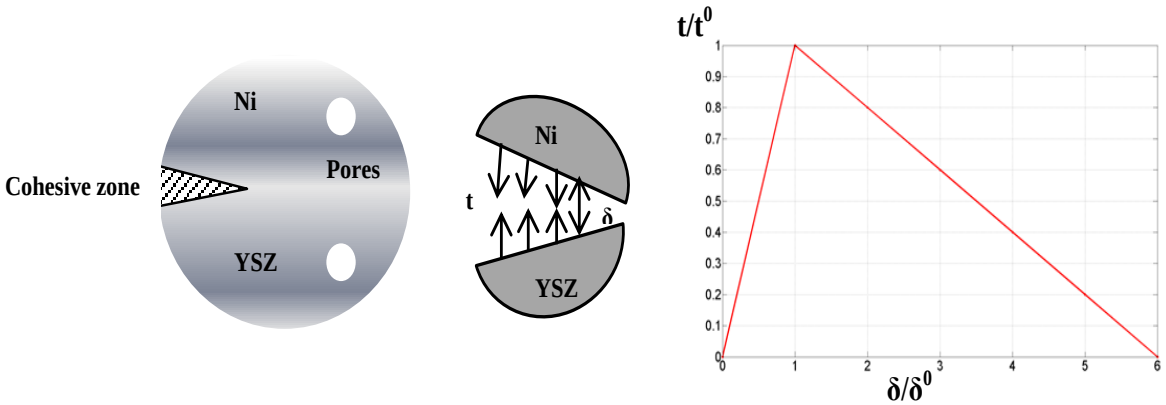


**Figure 4-2** Cohesive zone concept: (left) cohesive zone; (center) traction and separation in the cohesive zone; (right) idealized traction-separation curve.

In three dimensions, the traction-separation model for cohesive elements consists of three deformation modes: one normal mode and two in-plane shear modes [31]. In the normal mode, the deformation is purely in a direction perpendicular to the plane of the interface. In the two in-plane shear modes, the deformation is parallel to the plane of the interface. Thus, for 3-D cohesive elements, the traction vector (***t***) has three components: one normal component (i.e. perpendicular to the plane of the interface), $t_n$, and two in-plane shear components, $t_s$ and $t_t$, parallel to the plane of the interface. The separation vector (***δ***) has three corresponding components, $\delta_n$, $\delta_s$, and $\delta_t$. The nominal strain components can then be written as follows [31]:

$$\varepsilon_n = \frac{\delta_n}{T_0}; \varepsilon_s = \frac{\delta_s}{T_0}; \varepsilon_t = \frac{\delta_t}{T_0} \qquad (4-1)$$

Here, $T_0$ is the initial thickness of the interface. If we set $T_0 = 1$, the nominal strain components become numerically equal to the corresponding separation components. This re-scaling can be achieved by defining the interface stiffness ($K_i$) as follows [31]:

$$K_i = \frac{E_i}{T_0} \qquad (4-2)$$

$E_i$ is the Young's modulus of the interface material and $T_0$ is the initial thickness of the interface. In this study, the weak interfaces between dissimilar solid phases are modeled using cohesive elements with linear elastic traction-separation behavior up to damage initiation, followed by linear stiffness degradation to simulate damage evolution, as shown in Figure 4-3. A linear stiffness degradation model has been used by Xiao et al. [32] to study the fracture behavior of ultra-high strength concrete. Thus, the linear damage evolution model may be appropriate for describing the degradation of SOFC electrode interfaces between dissimilar solid (ceramic) phases that exhibit brittle behavior. The normal and in-plane modes of the traction-separation model used in this study are assumed to be uncoupled. The uncoupled linear elastic constitutive behavior of the cohesive elements can be expressed as follows, in terms of tractions ***t*** and separations ***δ*** (which are numerically equal to strains ***ε***) [31]:

$$\boldsymbol{t} = \begin{Bmatrix} t_n \\ t_s \\ t_t \end{Bmatrix} = \begin{bmatrix} K_{nn} & 0 & 0 \\ 0 & K_{ss} & 0 \\ 0 & 0 & K_{tt} \end{bmatrix} \begin{Bmatrix} \varepsilon_n \\ \varepsilon_s \\ \varepsilon_t \end{Bmatrix} = \boldsymbol{K_i \varepsilon} \qquad (4-3)$$

The uncoupled behavior of the cohesive elements is indicated by the fact that all off-diagonal terms are zero in the interface stiffness ($\boldsymbol{K_i}$) matrix in the constitutive traction-separation ($\boldsymbol{t}$-$\boldsymbol{\delta}$) relation given above. Figure 4-3 is a schematic representation of the traction-separation curve for LSM/YSZ interface cohesive elements used in this study. In Figure 4-3, $\delta^0$ is the critical separation at which damage is initiated in the cohesive element. Similarly, $\delta^f$ is the final separation at ultimate failure of the cohesive element.

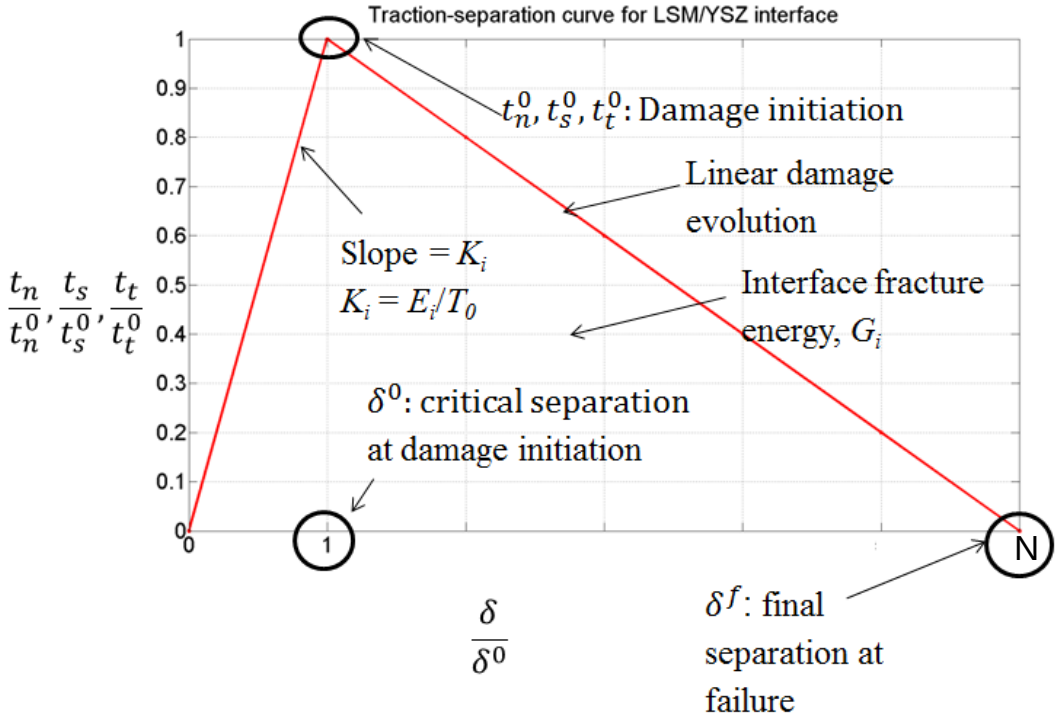


**Figure 4-3** Schematic diagram of traction-separation curve for an interface

Based on the approach adopted by Nguyen *et al*. [33], a quadratic stress interaction equation is used to describe the damage initiation condition [31]:

$$\left(\frac{\langle t_n \rangle}{t_n^0}\right)^2 + \left(\frac{t_s}{t_s^0}\right)^2 + \left(\frac{t_t}{t_t^0}\right)^2 = 1 \qquad (4-4)$$

Here, $t_n^0, t_s^0, t_t^0$ denote the maximum nominal stress when the deformation is either purely in a direction perpendicular to the plane of the interface or in one of the two orthogonal directions lying in the plane of the interface. The Macaulay brackets < > enclosing $t_n$ indicate that only tensile normal stress causes damage initiation in the cohesive elements. Purely compressive normal stress causes no damage in the cohesive layer [31]. This equation is used to describe the damage initiation criterion for the interface, accounting for the interaction between the normal (tensile) and in-plane (shear) stresses. Due to lack of detailed experimental data on the strength and stiffness properties of the NiO/YSZ and LSM/YSZ interfaces, the approach used by Nguyen *et al*. [33] is adopted for the cathode: the normal tensile strength and in-plane shear strengths of the LSM/YSZ interface are all assumed to be equal to the Weibull strength of the weaker phase (LSM), i.e. 52 MPa [9]. The stiffness of the LSM/YSZ interface is assumed to be characterized by the Young's modulus of LSM (40 GPa) [12]. Stiffness degradation does not occur for the cohesive elements under pure normal compressive stress.

The definitions of damage evolution used in this study are based on the fracture energies of the Ni/YSZ interface (anode) and the LSM/YSZ interface (cathode). The fracture energy (per unit interface area) is the area under the traction-separation curve for the interface. The critical energy release rate ($G_i$) for the LSM/YSZ interface is taken as 7.80 J m$^{-2}$ [15]. Based on numerical simulation results reported in the literature [15], the interface is assumed to fail in pure Mode I (normal mode) loading conditions. This leads to a mode-mix ratio $\psi$ = 0º, based on traction components. The Young's modulus and original thickness of the LSM/YSZ interface are used to calculate its normalized stiffness $K_i$ (40 x 10$^9$ N mm$^{-3}$). The stiffness $K_i$ and interface strength are used to calculate the critical separation $\delta^0$ (0.0013 nm). The area under the traction-separation curve is equal to the fracture energy per unit interface area, 7.80 J m$^{-2}$. This is used to calculate the final separation at ultimate failure, $\delta^f$ (0.3 μm).

For the anode, the normal tensile strength and in-plane shear strengths of the Ni/YSZ interface are all taken equal to the Weibull strength of NiO/YSZ reported in the literature (187 MPa) [9], due to lack of experimental data on the Ni/YSZ interface. The stiffness of the Ni/YSZ interface is assumed to be

characterized by the Young's modulus of YSZ (205 GPa) [12]. The critical energy release rate $G_i$ for the Ni/YSZ interface (28.10 J $m^{-2}$) is calculated as the area under its traction-separation curve, using the interface strength (187 MPa) and assuming that the final separation at failure $\delta^f$ is the same as that for the LSM/YSZ interface. The stiffness $K_i$ of the Ni/YSZ interface is then calculated from the assumed Young's modulus and original thickness of the cohesive layer, and $K_i$ is used to calculate $\delta^0$, as explained earlier. The Ni/YSZ interface also is assumed to fail in pure Mode I loading conditions. This again leads to a mode-mix ratio $\psi$ = 0º, based on traction components.

*4.2.2. Interface degradation scheme*

Degradation of the interface and TPB zones between dissimilar solid phases under repeated thermal cycling may be one of the major reasons for degradation of SOFC performance over time. In this study, interface degradation with thermal cycling is simulated using a simplified scheme. Only the heating phase of the thermal cycle is simulated. Steady-state conditions are assumed and transient effects are neglected. The models are subjected to five successive steady-state heating operations. Each analysis utilizes a spatially uniform temperature field to simulate steady-state heating of the model from room temperature (20 $^0$C) up to operating temperature (820 ºC). Progressive interface degradation is simulated by decreasing the stress at which damage begins in the cohesive interface layers in each successive analysis. The critical and final separations for the cohesive elements are assumed to remain unchanged over the five heating cycles, leading to a progressive reduction of both interface stiffness and critical energy release rate, as shown schematically in Figure 4-4.

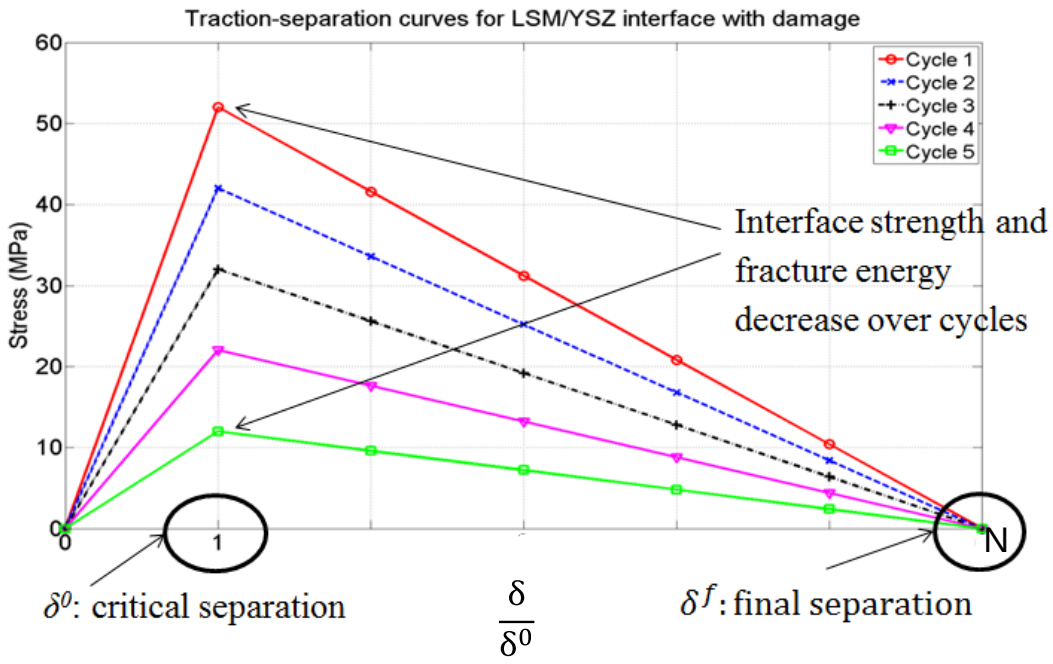


**Figure 4-4** Schematic diagram of interface degradation model

Critical energy release rate (i.e. fracture energy per unit interface area) is a measure of the resistance of the interface material to damage [34], while stiffness is indicative of the amount of damage (i.e. stiffness decreases as damage progresses) [34]. Therefore, both stiffness and fracture energy are assumed to progressively decrease with thermal cycling. Thus, this scheme implements interface degradation in a simplified manner. Mechanical degradation of the interface is considered, without considering interface degradation due to electrochemical or redox processes. The above scheme is only a first approximation to the complex degradation processes that occur at the actual interfaces in a real SOFC electrode. Multiphysics simulations considering both mechanical and electrochemical degradation processes may be an interesting topic for future research.

### 4.3. Study design

In the first part of this study, two sets of electrode microstructure models are generated. One set has perfect bonding throughout the entire model, and the other has cohesive zones between dissimilar solid phases. Image-based 3-D models similar to those described in previous chapters are used here, with one important difference. The models used in Chapter 3 are derived through image simplification by analyzing (2 × 2) pixel squares in the original images. This scheme increases the effective pixel size, but preserves both the overall size of the image and the depth of the voxel, leading to a decrease in the reconstructed volume due to the use of a limited number of images. However, this scheme leads to a reasonably good approximation of the original microstructure, as validated in Chapter 3. In the present study, a similar approach is used to simplify the model. An algorithm is devised to analyze consecutive pixel squares of ($n \times n$) pixels in each original image. For each such square, the number of pixels belonging to each phase is counted. The phase that contributes the maximum number of pixels to the $n \times n$ pixel square is assigned as the final phase of the single pixel at that location in the simplified image. Additionally, in the present approach, preservation of the original volume of the electrode model in the simplified version is implemented by causing an increase in both effective pixel size and effective voxel depth. The volumes of the simplified models used here are 112.18 $\mu m^3$ for the anode and 670.35 $\mu m^3$ for the cathode. The cathode volume may be compared against the sampled volume of 178 $\mu m^3$ for the simplified cathode model described in Chapter 3. The values of $n$ used in this study are as follows: for the cathode, $n$ = 6, and for the anode, $n$ = 10. These levels of simplification are necessary to achieve reasonable computational time for each FE analysis (8-10 hours for cathode and 15-20 hours for anode). A detailed validation study for this new approach based on volume fractions, phase surface area densities, and TPB densities may be an interesting topic for future research. In the present study, the plausibility of this new approach is demonstrated by showing that TPB density values obtained for anode and cathode models lie within physically reasonable limits of experimentally determined ranges for these values.

Increasing levels of thermal load are applied through spatially uniform temperature fields of magnitude 120 $^0$C, 220 $^0$ C,…, 820 $^0$C, to simulate steady-state heating from room temperature (20 $^0$C) up to operating temperature. Energy quantities (e.g. strain energy and damage dissipation) are calculated from FEA for each $\Delta T$ = 100 $^0$C, 200 $^0$C,…, 800 $^0$C. The energy quantities for models with and without cohesive zones are compared to gain insight into the effect of weak interface zones between dissimilar solid phases on the mechanical integrity of the cathode. Energy concepts from fracture mechanics are used to interpret the results obtained. This procedure is performed using the cathode microstructure model, considering the original composition (50:50 wt. % LSM:YSZ).

In the second part of the study, three-phase boundary (TPB) evolution under repeated, steady-state, monotonic thermal loads is studied using 50:50 wt. % electrode microstructure models. Electrode models with cohesive interface zones are subjected to five successive monotonic, steady-state, heating operations from room temperature up to operating temperature ($\Delta T$ = +800 $^0$C) using a spatially uniform temperature field. During each successive analysis, the strength of the cohesive interface between dissimilar solid phases is decreased to simulate the effect of interface degradation under thermal cycling. Progressive interface degradation under thermal cycling is implemented using the simplified scheme explained earlier in this chapter. The strains induced in the cohesive layers are calculated using FEA and are used to quantify TPB zone damage using a strain-based criterion, i.e. separation in the cohesive layers, as explained later.

### 4.4. Analysis, results, and discussion: energy quantities

#### *4.4.1. Analysis procedure*

Cohesive elements give rise to numerical convergence and stability issues that are well-documented in the technical literature, e.g. [31]. Unstable behavior of cohesive elements due to negative stiffness (i.e. softening) in the damage evolution phase causes local instability in the electrode models used in this study. The local stabilization algorithm available in Abaqus v6.11 [31] is used along with viscous regularization [31] for the cohesive elements to address convergence and stability issues. Small values of the viscosity parameter ($\mu = 0.001 – 0.01$) are used to ensure that the energy quantities dissipated in regularization and stabilization are small compared with the strain energy in the model. Fixed boundary conditions (BCs) are prescribed by fixing all degrees of freedom (DOFs) at each node on each face of the models. The 3-D cathode model with cohesive zones is subjected to steady-state temperature change from room temperature (20 ºC) up to operating temperature. Spatially uniform temperature fields of increasing magnitude (120 ºC, 220 ºC,…, 820 ºC) are used to apply increasing levels of thermal load ($\Delta T$ = 100 ºC, 200 ºC,…, 800 ºC). Similar analyses are performed for the 3-D cathode model without cohesive zones. Energy quantities (e.g. strain energy and damage dissipation) are computed from each FE analysis.

#### *4.4.2. Results*

The cathode microstructure model (with cohesive elements) used in this phase of the study is shown in Figure 4-5. Figure 4-5 also shows the horizontal and vertical interface zones between dissimilar solid phases that are composed of cohesive elements. The vertical interface zone cohesive elements are shown using the anode microstructure model utilized in the second phase of this study involving repeated thermal loading. The concept of horizontal and vertical interface zones implemented in the FE models used in this study is further illustrated through the schematic diagram shown in Figure 4-6.

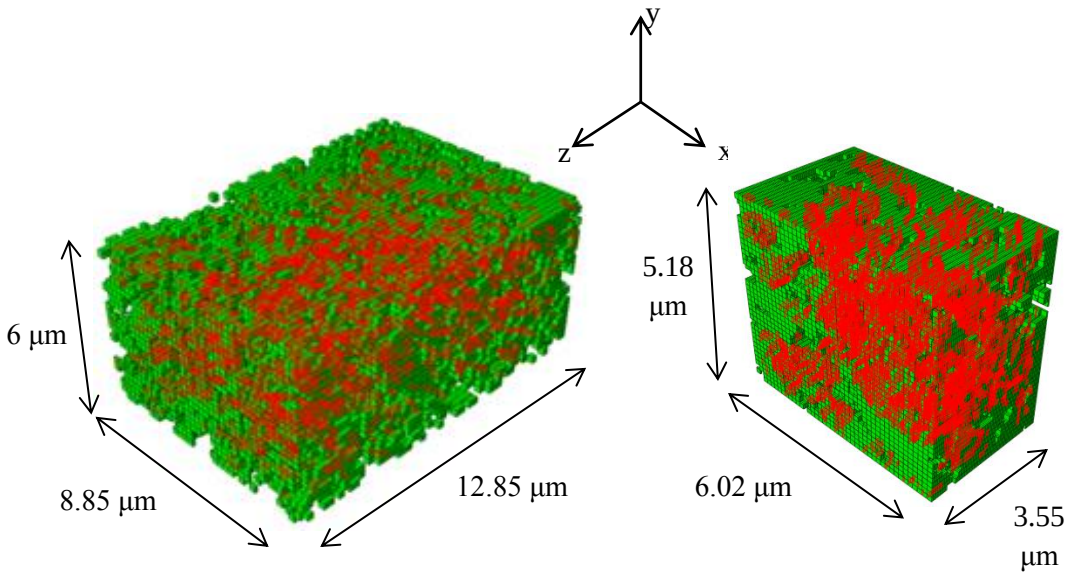


**Figure 4-5** (left) Cathode model with horizontal interface zones; (right) anode model with vertical interface zones

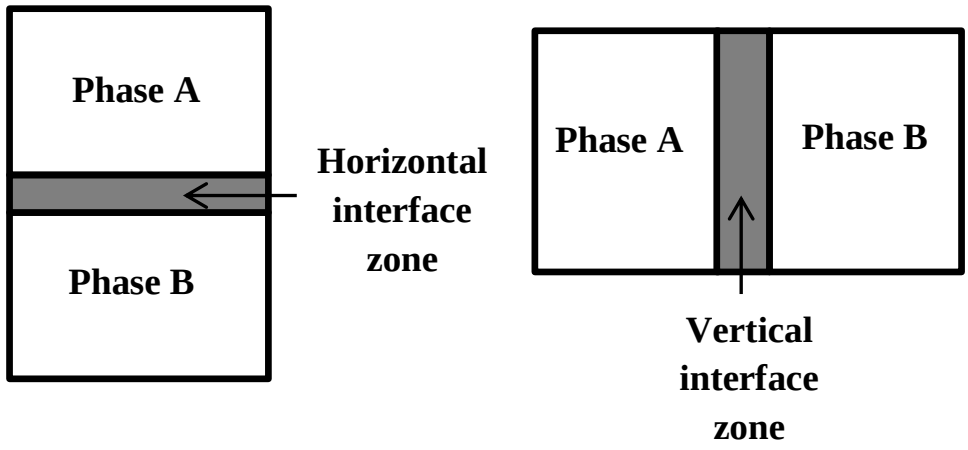


**Figure 4-6** Schematic diagram of horizontal and vertical interface zone concepts

Figure 4-7 is a graphical plot showing a comparison of energy quantities obtained from the FE analyses of cathode models with and without cohesive interface zones. The energy quantities are plotted as functions of temperature in Figure 4-7, which shows a comparison between the strain energies of the cohesive model and the non-cohesive model. The energy dissipated due to damage (i.e. the damage dissipation) in the interface zones of the cohesive cathode model is plotted as a function of temperature in Figure 4-8.

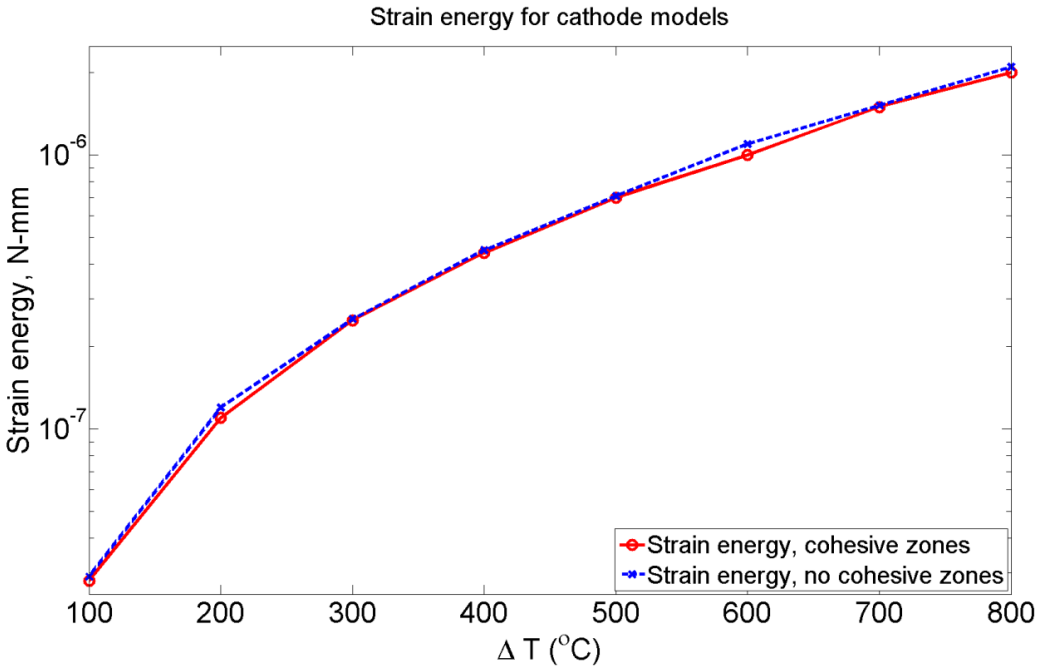


**Figure 4-7** Strain energy in cathode models with and without cohesive interface zones

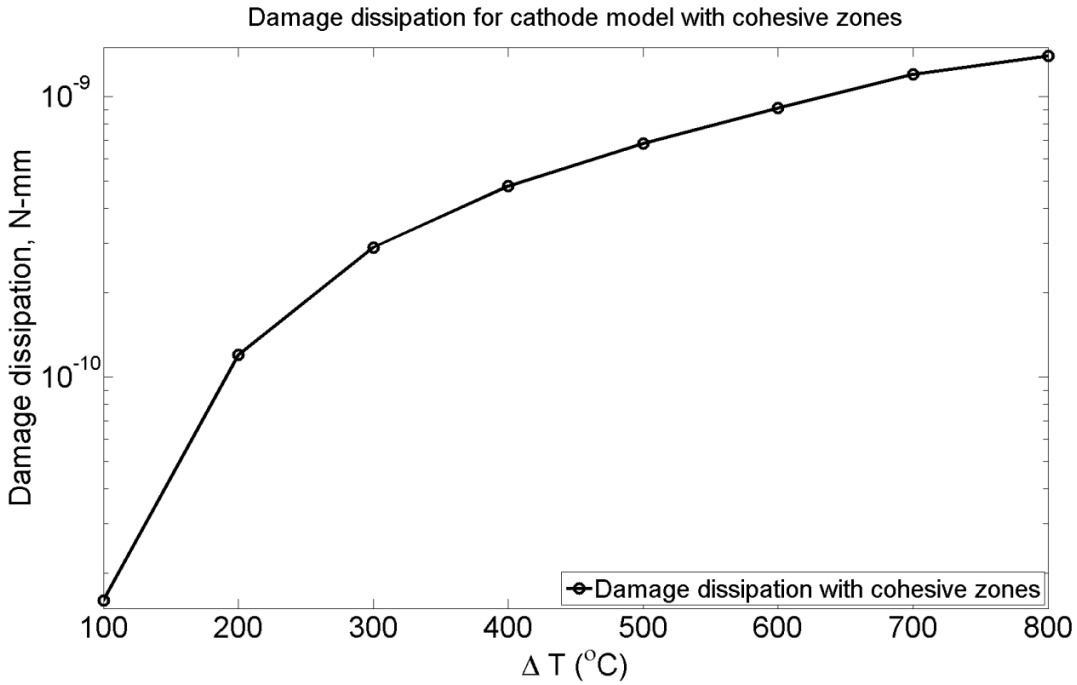


**Figure 4-8** Damage dissipation in cathode model with cohesive zones

*4.4.3. Discussion*

It is observed from Figure 4-7 that the strain energy of the cohesive and non-cohesive cathode models increases with increasing temperature, as expected from the larger thermal stresses induced at higher temperatures, with fixed boundary conditions. Similarly, from Figure 4-8, it is seen that the energy dissipated due to interfacial damage in the cohesive model also increases with increasing temperature, since more damage occurs at higher temperatures. A significant feature of Figure 4-7 is that the strain energy of the non-cohesive model is slightly higher than that of the cohesive model at all temperatures. The strain energy and damage dissipation for all ΔT values are given in Table 4-1. Table 4-1 also compares the strain energy values for the cohesive model and non-cohesive model. At a given temperature, the strain energy of the cohesive model is lower than that of the non-cohesive model, due to damage dissipation in the interface zones of the cohesive model.

**Table 4-1** Cathode model: strain energy and damage dissipation data (CZM = cohesive zone model)

| ΔT (ºC) | Strain energy, CZM ($10^{-8}$ N-mm) | Damage dissipation, CZM ($10^{-8}$ N-mm) | Strain energy, non-CZM ($10^{-8}$ N-mm) |
|---|---|---|---|
| 100 | 2.851 | 0.0016 | 2.856 |
| 200 | 11.41 | 0.0121 | 11.46 |
| 300 | 25.07 | 0.0287 | 25.18 |
| 400 | 44.54 | 0.0478 | 44.76 |
| 500 | 70.55 | 0.0678 | 70.92 |
| 600 | 105.4 | 0.0909 | 106.0 |
| 700 | 150.5 | 0.1171 | 151.4 |
| 800 | 205.4 | 0.1446 | 206.6 |

The physical explanation of the above observations is as follows. From the first law of thermodynamics and the Griffith energy balance statement for fracture (i.e. damage), we know that a damage process (e.g. cracking) can occur in a system only if this process causes the total energy of the system to either decrease or remain constant [35]. The limiting condition is attained when damage occurs at equilibrium conditions, with the total energy remaining constant [35]:

$$\frac{dE}{dA} = \frac{d\Pi}{dA} + \frac{dW_s}{dA} = 0 \qquad (4-5)$$

Here,

E = total energy of the system,

Π = potential energy of the system = U – F,

U = strain energy of the system,

F = work done by external forces,

$W_s$ = work required for creating new surfaces,

A = damage variable (e.g. crack length)

In the cathode models analyzed, fixed boundary conditions are prescribed. This means that all translational and rotational DOFs at each node on each face of the model are set to zero. Thus, this model can be regarded as a displacement controlled model [35], with the displacement of the faces fixed at zero. For a displacement controlled system, we know that the external work is zero (F = 0) [35]. This is

confirmed by the numerical values of the external work obtained from FEA, which are on the order of $10^{-40}$. Thus, for a displacement controlled system, Π = U. Finally, from Irwin's energy release rate analysis [35], we know that for displacement control the strain energy of the system decreases as damage (e.g. cracking) occurs. This explains the lower strain energy of the cohesive model as compared to the non-cohesive model at a given temperature.

### 4.5. Analysis, results, and discussion: three-phase boundary (TPB) evolution

#### *4.5.1. Analysis procedure*

The main objective of this phase of the study is to approximately simulate the effects of thermal cycling on electrode integrity and performance using monotonic, steady-state, thermal loads coupled with an interface strength degradation scheme. In order to achieve this objective, the electrode models (cathode: 50:50 wt. % LSM:YSZ, anode: 50:50 wt. % NiO:YSZ) with cohesive zones are subjected to five successive analyses. Each analysis represents the heating phase of a normalized thermal cycle, with one normalized cycle being taken equal to 1000 cycles. Only the heating phase of the thermal cycle is simulated in each analysis. Steady-state conditions are assumed and transient effects are neglected. Starting from a uniform initial room temperature of 20 ºC, the models are subjected to steady-state temperature change up to an operating temperature of 820 ºC using a spatially uniform temperature field. During each successive analysis, progressive interface degradation is simulated by decreasing the interface strength and fracture energy of the cohesive layers, as explained in subsection 4.2.2. Two separate interface strength degradation schemes are studied. In the first scheme (Scheme 1), the initial interface strength is assumed to decrease by 5 MPa in each successive cycle. In the second scheme (Scheme 2), the interface strength is assumed to decrease by 10 MPa in each successive cycle. The constitutive thickness of each cohesive element is set equal to 1.0, so that the nominal strain components ($\varepsilon$) calculated using FE analysis are numerically equal to the respective separation components ($\delta$). Figure 4-9 shows the interface strength reduction schemes employed to study TPB evolution in the cathode under repeated thermal loading. Figure 4-9 illustrates both Scheme 1 ($\Delta t_i^0$ = -5 MPa per cycle, where $t_i^0$ = interface strength) and Scheme 2 ($\Delta t_i^0$ = -10 MPa per cycle).

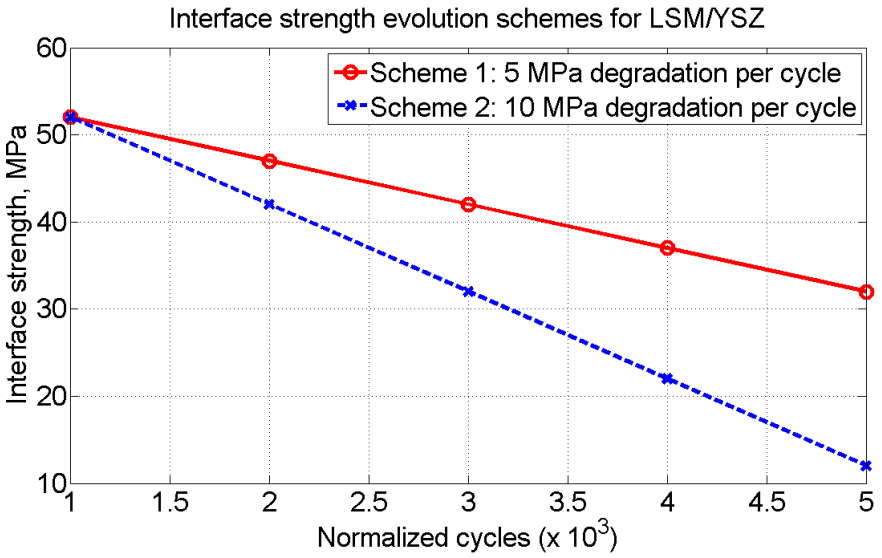


**Figure 4-9** Interface strength evolution schemes: LSM/YSZ interface

The numerical values of interface strength and fracture energy used in Scheme 1 ($\Delta t_i^0$ = -5 MPa per cycle) and Scheme 2 ($\Delta t_i^0$ = -10 MPa per cycle) are given in Tables 4-2 and 4-3 below.

**Table 4-2** Anode model: interface strength and fracture energy data

| Normalized cycles (x $10^3$) | Interface strength, MPa (Scheme 1) | Interface strength, MPa (Scheme 2) | Interface fracture energy, J $m^{-2}$ (Scheme 1) | Interface fracture energy, J $m^{-2}$ (Scheme 2) |
|---|---|---|---|---|
| 1 | 187 | 187 | 28.10 | 28.10 |
| 2 | 182 | 177 | 27.30 | 26.60 |
| 3 | 177 | 167 | 26.60 | 25.10 |
| 4 | 172 | 157 | 25.80 | 23.60 |
| 5 | 167 | 147 | 25.10 | 22.10 |

**Table 4-3** Cathode model: interface strength and fracture energy data

| Normalized cycles (x $10^3$) | Interface strength, MPa (Scheme 1) | Interface strength, MPa (Scheme 2) | Interface fracture energy, J $m^{-2}$ (Scheme 1) | Interface fracture energy, J $m^{-2}$ (Scheme 2) |
|---|---|---|---|---|
| 1 | 52 | 52 | 7.80 | 7.80 |
| 2 | 47 | 42 | 7.05 | 6.30 |
| 3 | 42 | 32 | 6.30 | 4.80 |
| 4 | 37 | 22 | 5.55 | 3.30 |
| 5 | 32 | 12 | 4.80 | 1.80 |

Pitakthapanaphong and Busso [15] have performed numerical simulations to determine the critical energy release rates ($G_i$) for several material interfaces encountered in SOFC systems. Numerically, these values vary from 7.80 J $m^{-2}$ for LSM/YSZ interface to 38.70 J $m^{-2}$ for LSM-LSCoO interface. From these data, it can be concluded that the interface fracture energy values used in this study (Tables 4-2 and 4-3) are physically reasonable.

Cathode and anode models with fixed boundary conditions (BCs) are used in this study. The models are subjected to repeated, monotonic, steady-state heating as explained above, and the thermal stresses and strains are calculated through FEA. The strains induced in each cohesive element are written to the output data file associated with each analysis, along with strain energy and damage dissipation values. The strains are used to calculate the evolution of three-phase boundaries (TPBs) with thermal cycling, as explained in the next subsection. The energy quantities are used to study the mechanical degradation of the overall model, as explained in section 4.4.

*4.5.1.1 Algorithm for calculating TPB evolution*

The TPB length at each temperature is calculated as follows. First, an electrode model without cohesive zones is created by image stacking (using a cell array data structure in MATLAB® [25]). The original 2-D images used to reconstruct the 3-D microstructure are stored as pixel value arrays in the cell array. In each 2-D image, boundary pixels are identified by pixel value comparison of each pixel with its 8 adjacent in-plane neighbors. Boundary pixels are stored as black pixels (pixel value = 0) at corresponding locations in an initially empty "boundary point" cell array of identical size as the image cell array. Interior (i.e. non-boundary) locations are stored as white pixels at corresponding locations in the boundary point cell array. Using the boundary point cell array, locations of boundary pixels in the image array are identified as black pixels in the boundary point array, and the pixel value of the boundary pixel at the corresponding location in the image array is checked. The pixel values of the 8 pixels adjacent to that boundary pixel are also checked to test whether all 3 phases are present at that boundary location. If so,

the location is stored as a three-phase boundary (TPB) point (black pixel) in another initially empty "TPB" cell array. All other non-TPB locations are stored as white pixels in the TPB array. After TPB locations have been identified, the total number of TPB points is counted, and multiplied by the z-distance between images, to obtain the total undamaged TPB length (μm) in the electrode models. The total undamaged TPB length (μm) is divided by the volume ($\mu m^3$) of the 3-D electrode model to obtain the TPB density ($\mu m^{-2}$) in the model.

For the cohesive models, the following scheme is used to determine the TPB length and density. From the TPB locations identified previously, the element numbers of the cohesive elements present at each TPB location are calculated and written to a text file. The data files obtained from the FE analyses of the cohesive models are used to extract the normal and in-plane strain components for each cohesive element. The strain components for each TPB cohesive element are then checked to determine whether the normal strain component is greater than zero (i.e. $\delta_n > 0$). If $\delta_n > 0$, then the TPB element is assumed to have failed, since the TPB length contributed by that element is lost. Figure 4-10 illustrates the undeformed and deformed states of such a failed TPB cohesive element in a horizontal interface zone between LSM and YSZ.

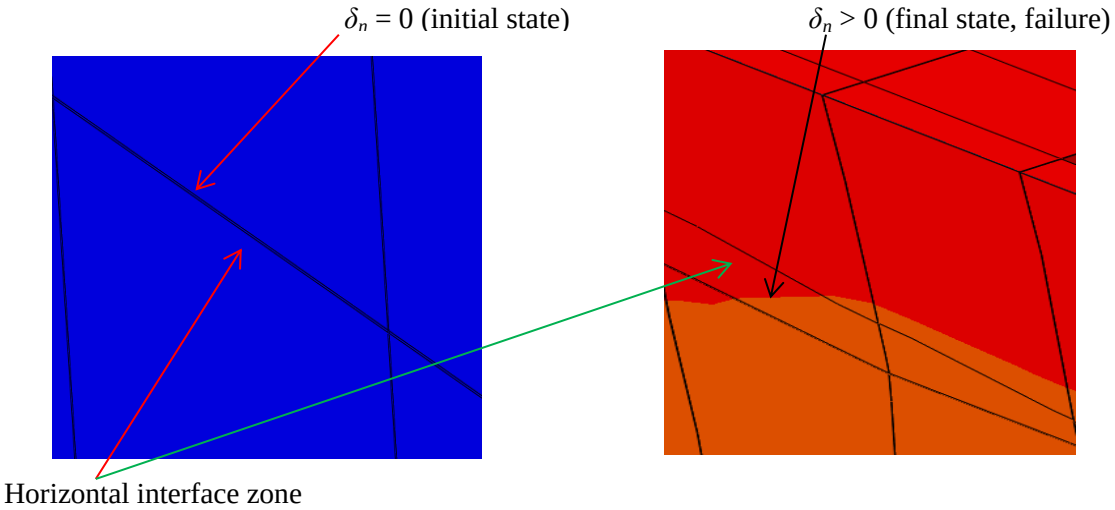


**Figure 4-10** Undeformed (left) and deformed (right) states of a failed cohesive element in a horizontal interface zone

Each time such a failed TPB cohesive element is located, a TPB damage counter (initially set to zero) is incremented by 1. The TPB loss in the model is quantified by calculating the total number of failed TPB cohesive elements, and multiplying the total number of failed elements by the z-distance. The damaged TPB length (μm) is calculated by subtracting the TPB loss from the undamaged TPB length. The damaged TPB density ($\mu m^{-2}$) is calculated by dividing the damaged TPB length (μm) by the volume ($\mu m^3$) of the 3-D electrode model.

Damage accumulation over 5 normalized cycles is calculated by determining the failed TPB cohesive elements in each cycle that had not failed in the previous cycle. The difference between the number of failed TPB elements in the $(n+1)^{th}$ cycle and in the $n^{th}$ cycle is used to quantify the additional TPB loss in each successive cycle, and the cumulative TPB loss over N such cycles is thus determined by successively adding the new damage in each cycle to the cumulative total damage over the previous (N-1) cycles. The model used in this study for evaluating cumulative TPB damage with thermal cycling may be regarded as a simple model for calculating cumulative fatigue damage. A detailed mathematical model for predicting the lifetime of planar SOFCs subjected to thermal cycling has been developed by Liu et al. [36]. That model uses Paris' law and crack nucleation concepts to derive expressions for damage distribution in the interfacial layers of planar SOFCs under thermal cycling. It predicts that the number of cycles required for failure will decrease with increase in electrolyte thickness and electrode porosity [36].

### *4.5.2. Results*

#### *4.5.2.1. Energy quantities*

Figure 4-11 depicts the change in the strain energy content of the cathode with thermal cycling. The figure shows that for both interface degradation schemes, the strain energy of the model progressively decreases over 5 normalized thermal cycles. This is expected from the progressive mechanical degradation of the interfaces within the model with thermal cycling.

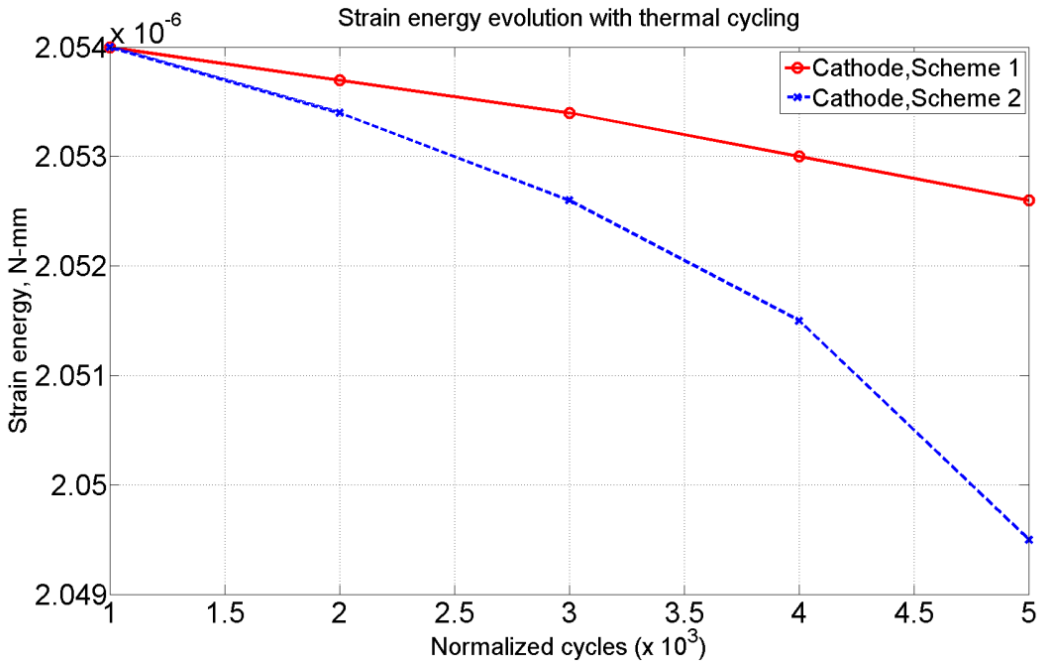


**Figure 4-11** Strain energy evolution for cathode model with thermal cycling

Such progressive interface degradation leads to a cumulative dissipation of energy due to damage, and hence to a progressive decrease in strain energy content of the model. This is further illustrated in Figure 4-12, which shows the cumulative damage dissipation with thermal cycling. As expected, Scheme 2 ($\Delta t_i^0 = -10$ MPa per cycle) leads to lower strain energy content, and larger cumulative damage dissipation, than Scheme 1 ($\Delta t_i^0 = -5$ MPa per cycle).

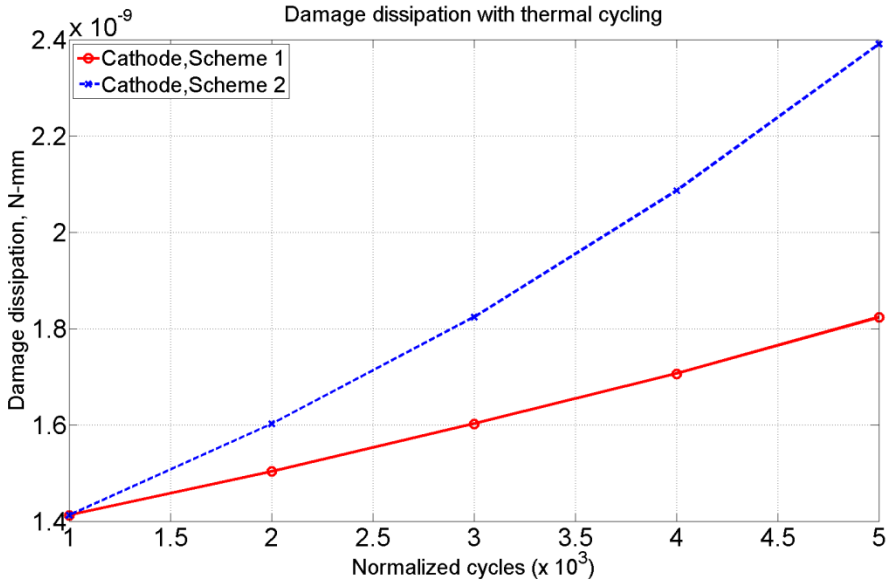


**Figure 4-12** Damage dissipation in cathode model with thermal cycling

*4.5.2.2. Three-phase boundary evolution*

Figure 4-13 shows the evolution of the TPB density with thermal cycling for the anode and cathode models considered in this study. This figure simultaneously compares the TPB density evolution for cathode versus anode, and for Scheme 1 ($\Delta t_i^0$ = -5 MPa per cycle) versus Scheme 2 ($\Delta t_i^0$ = -10 MPa per cycle). The numerical values of TPB length and TPB density for the anode and cathode models are summarized in Tables 4-4 and 4-5 below.

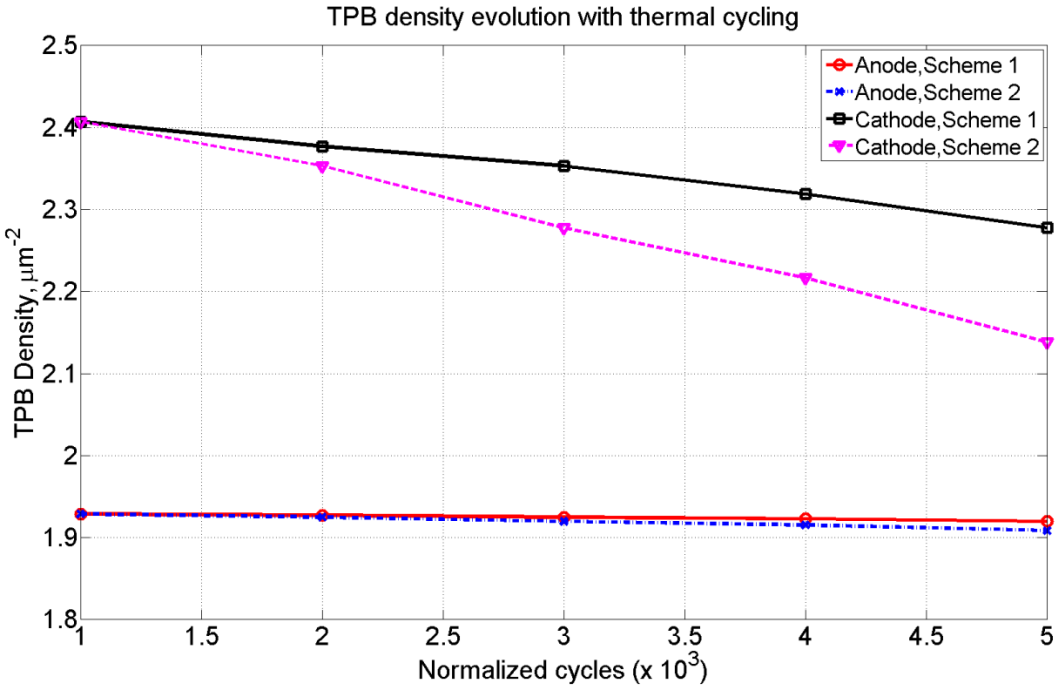


**Figure 4-13** TPB density evolution with thermal cycling for electrode models

**Table 4-4** Anode model: TPB length and TPB density evolution data

| Normalized cycles (x $10^3$) | TPB length, Scheme 1 (μm) | TPB length, Scheme 2 (μm) | TPB density, Scheme 1 ($\mu m^{-2}$) | TPB density, Scheme 2 ($\mu m^{-2}$) |
|---|---|---|---|---|
| 1 | 216.38 | 216.38 | 1.929 | 1.929 |
| 2 | 216.20 | 215.94 | 1.927 | 1.925 |
| 3 | 215.94 | 215.36 | 1.925 | 1.920 |
| 4 | 215.72 | 214.88 | 1.923 | 1.916 |
| 5 | 215.36 | 214.12 | 1.920 | 1.909 |

**Table 4-5** Cathode model: TPB length and TPB density evolution data

| Normalized cycles (x $10^3$) | TPB length, Scheme 1 (μm) | TPB length, Scheme 2 (μm) | TPB density, Scheme 1 ($\mu m^{-2}$) | TPB density, Scheme 2 ($\mu m^{-2}$) |
|---|---|---|---|---|
| 1 | 1613.60 | 1613.60 | 2.407 | 2.407 |
| 2 | 1593.40 | 1577.40 | 2.377 | 2.353 |
| 3 | 1577.40 | 1526.80 | 2.353 | 2.278 |
| 4 | 1554.40 | 1485.80 | 2.319 | 2.217 |
| 5 | 1526.80 | 1433.30 | 2.278 | 2.138 |

*4.5.3. Discussion*

Figure 4-13 shows that the TPB density of anode and cathode models decreases over the 5 successive normalized thermal cycles ($\Delta T = +800$ ºC), as expected from the progressive degradation of the interface with thermal cycling. As expected for both anode and cathode models, Scheme 2 (10 MPa degradation per cycle) leads to a lower final TPB density than Scheme 1 (5 MPa degradation per cycle), after 5 normalized heating cycles. The TPB density of the cathode undergoes a larger reduction (5.36 % for Scheme 1, 11.18 % for Scheme 2) than the TPB density of the anode (0.47 % for Scheme 1, 1.04 % for Scheme 2). This is expected from the physical properties of the Ni/YSZ and LSM/YSZ interfaces. The anode (Ni/YSZ) interface has higher strength (187 MPa) compared with the cathode (LSM/YSZ) interface (52 MPa). The Ni/YSZ interface also has higher damage resistance ($G_i$ = 28.10 J m$^{-2}$) than the LSM/YSZ interface ($G_i$ = 7.80 J m$^{-2}$). It may be noted from Figure 4-13 that the cathode has higher TPB density than the anode. This fact has been experimentally observed by Wilson *et al.* [5] who point out that TPB density may be higher for cathodes than for anodes due to the finer cathode microstructures. Wilson *et al.* [20] have cited TPB density values lying in the range of 1.7 – 6.5 μm$^{-2}$ for cathodes and have reported cathode TPB density values in the range of 6 – 9 μm$^{-2}$ [5]. For anodes, values ranging from 2.40 – 4.28 μm$^{-2}$ have been reported [4, 19]. From these experimental data, it may be concluded that the TPB density values obtained in this study for cathode (2.138 – 2.407 μm$^{-2}$) and anode (1.909 – 1.929 μm$^{-2}$) are physically reasonable.

**4.6. Conclusion**

The effect of interface degradation under repeated thermal loading on mechanical integrity and electrochemical performance of SOFC electrodes is simulated by implementing a simplified damage scheme in anode and cathode FE models with cohesive interface zones. The cathode model is first subjected to increasing levels of thermal load using spatially uniform temperature fields. Energy quantities for models with and without cohesive interface zones are obtained through FEA. These quantities are compared using energy balance concepts from fracture mechanics to gain insight into the

effects of interface degradation on mechanical integrity. The effect of interface degradation with increasing temperature on the mechanical integrity of a displacement controlled cathode microstructure model is clearly seen as a reduction in strain energy of the model due to damage dissipation. The evolution of three-phase boundary (TPB) zones in electrode microstructure models with thermal cycling is studied by implementing an interface damage scheme that includes reduction of both interface strength and fracture energy. It is found that TPB density decreases over a number of normalized heating cycles. Degradation of the mechanical integrity of the cathode model under repeated thermal loading is also observed, in the form of progressively decreasing strain energy content due to cumulative damage dissipation with thermal cycling. These observations indicate that interface damage may be a major mechanism responsible for SOFC performance degradation over time.

# Chapter 5

# Conclusion

## 5.1. Concluding remarks

The five objectives of the research presented in this dissertation are identified in the introductory chapter (Chapter 1).These objectives have provided a guideline for the work presented in Chapters 2, 3, and 4. Reconstruction of three-dimensional FE models of SOFC anode microstructures from stacks of two-dimensional images of actual anode cross-sections is described in Chapter 2 (Objective 1). Finite element thermal stress analysis of the models under spatially uniform temperature fields of increasing magnitude is also described in Chapter 2, where the effects of temperature-dependent material properties and plasticity are investigated (Objectives 2 and 3). Weibull analysis of thermal stresses is performed to determine the probability of failure of the anode microstructure as a function of temperature. The Weibull analyses show that the linear elastic material models underestimate the probability of failure of the anode at high temperatures. Hence, it is important to consider the nonlinear behavior of the nickel phase of the Ni-YSZ anode.

In Chapter 3, finite element thermal stress analyses of microstructure-based SOFC cathode models are described. The effects of temperature-dependent material properties and varying phase volume fractions of cathode materials on the behavior of the cathode microstructure under thermal loads are investigated (Objective 4). An approximate heuristic volume fraction modification scheme is developed and validated. This scheme is based on boundary pixel modification of original 50:50 wt. % LSM:YSZ microstructure images, and is used to derive a microstructure of 30:70 wt.% LSM:YSZ composition. Construction of derived microstructures using such heuristic schemes may provide a simplified, approximate approach for investigating the effects of phase compositions on the mechanics of electrode structures. The scheme is approximate in nature and is not intended to replace more rigorous approaches such as the random packing model. The important results are as follows. First, consideration of temperature-independent material properties of the SOFC cathode materials results in higher probability of failure values than those

obtained with temperature-dependent material properties. Second, limited variations in the volume fractions of LSM and YSZ phases have limited effect on probability of failure of models with temperature-independent material properties. However, higher pore volume fraction does lead to higher probability of failure due to the stress concentration effect of pores. With temperature-dependent material properties, the cathode model with higher volume fraction of YSZ is found to have lower stresses and lower probability of failure, due to the decrease in the Young's modulus of YSZ with increasing temperature.

Chapter 4 describes the methods used to investigate the effects of interface degradation under repeated thermal loading on the mechanical integrity and electrochemical performance of SOFC electrodes (Objective 5). Cohesive interface zones between dissimilar solid phases are used to implement a simplified damage model. The effect of interface degradation on mechanical integrity is studied by subjecting 50:50 LSM:YSZ wt. % cathode models to increasing levels of thermal load from room temperature up to operating temperature. Energy quantities obtained through FEA are analyzed using energy balance concepts from fracture mechanics to gain insight into the effects of interface degradation on mechanical integrity. The effect of interface degradation with increasing temperature on the mechanical integrity of a displacement controlled model is clearly seen as a reduction in strain energy of the model due to damage dissipation. Electrochemical performance degradation of SOFC with thermal cycling due to reduction in three-phase boundary (TPB) density is also investigated in Chapter 4. Interface degradation under repeated thermal loading is implemented in the FE electrode models through a simplified scheme. TPB evolution due to progressive interface damage is evaluated in a simplified manner, by considering only mechanical degradation of the interface due to repeated thermal loading. Electrochemical and redox cycling are not considered in evaluating interfacial damage. It is found that TPB density decreases over a number of normalized heating cycles, indicating that interface damage may be a major mechanism responsible for SOFC performance degradation over time.

### 5.2. Limitations of the study and suggestions for future work

The finite element analyses performed in this work are limited to steady-state phenomena. The effects of transient loads on the mechanical integrity of electrode microstructure models may be an interesting topic for future research. Residual stresses are not considered in the modeling performed in this work, due to lack of such experimental data. It may be interesting to consider residual stresses in future modeling efforts. Spatially uniform temperature fields are considered in this work. Spatially non-uniform temperature fields could be considered in future work on SOFC modeling. Finally, the interface degradation scheme used in this work considers only mechanical damage to the interface zones. Detailed numerical simulations considering interfacial damage due to multiple mechanisms such as electrochemical reactions, redox cycling, and thermal cycling, may be a very interesting topic for future research.

The thermal stress and probability of failure analyses presented in Chapters 2 and 3 investigate the effects of factors such as temperature-dependent material properties, elastic-plastic behavior, and phase volume fractions on the integrity of the SOFC electrodes. The results presented in these chapters correlate material and microstructure properties, as well as material behavior, with the probability of failure. More specifically, the results presented in Chapter 3 correlate properties of the microstructure, e.g. pore and solid phase volume fractions, with the probability of failure. Multi-scale studies involving computational simulations and actual experiments may be necessary to correlate the results of the microstructure-based probability of failure analyses reported in Chapters 2 and 3 with the results of studies on full-scale SOFCs. Such studies, after rigorous experimental validation, may be of assistance in framing materials selection guidelines for the designers of SOFCs in the future. These studies may also guide researchers investigating the optimization of SOFC microstructures. Such optimized microstructures may offer better electrochemical performance without compromising structural and mechanical integrity.

The work presented in Chapter 4 employs a highly simplified simulation of thermal fatigue. This thermal fatigue analysis investigates the effect of repeated steady-state thermal loading on the integrity of interfaces, especially three phase boundary zones. Electrochemical performance degradation of the SOFC electrodes under thermal fatigue is evaluated by studying three phase boundary evolution over a number of normalized heating cycles. Experimental studies on SOFC performance degradation under different cycling conditions, such as those conducted by Dikwal *et al.* [37] and Bujalski *et al.* [38] are very useful in quantifying the decrease in electrochemical performance of SOFCs over time. Such studies may be useful for validating the predictions of performance degradation simulations on computational models of full-scale SOFCs under various cycling conditions. Finally, the literature in this field would also benefit greatly from experimental investigations correlating SOFC performance degradation with microstructure evolution (e.g. TPB evolution) under various cycling conditions. Such studies are required for validating the results of thermal fatigue modeling efforts such as those reported in Chapter 4 of this work.

## References


[1] S. C. Singhal, K. Kendall (Eds.), High-temperature Solid Oxide Fuel Cells: Fundamentals, Design and Applications: Fundamentals, Design and Applications, Elsevier; 2003.

[2] A. Selimovic, M. Kemm, T. Torisson, M. Assadi, Steady state and transient thermal stress analysis in planar solid oxide fuel cells, Journal of Power Sources, 145 (2005) 463-469.

[3] G. Anandakumar, N. Li, A. Verma, P. Singh, J. Kim, Thermal stress and probability of failure analyses of functionally graded solid oxide fuel cells, Journal of Power Sources, 195 (2010) 6659-6670.

[4] J.R. Wilson, S.A. Barnett, Solid oxide fuel cell Ni-YSZ anodes: effect of composition on microstructure and performance, Electrochemical and Solid-State Letters, 11 (2008) B181-B185.

[5] J.R. Wilson, J.S. Cronin, A.T. Duong, S. Rukes, H. Chen, K. Thornton, D.R. Mumm, S. Barnett, Effect of composition of ($La_{0.8}Sr_{0.2}MnO_3$-$Y_2O_3$-stabilized $ZrO_2$) cathodes: correlating three-dimensional microstructure and polarization resistance, Journal of Power Sources, 195 (2010) 1829-1840.

[6] R. Clague, P. Shearing, P. Lee, Z. Zhang, D. Brett, A. Marquis, N. Brandon, Stress analysis of solid oxide fuel cell anode microstructure reconstructed from focused ion beam tomography, Journal of Power Sources, 196 (2011) 9018-9021.

[7] A. Selçuk, A. Atkinson, Elastic properties of ceramic oxides used in solid oxide fuel cells (SOFC), Journal of the European Ceramic Society, 17 (1997) 1523-1532.

[8] A. Selçuk, A. Atkinson, Strength and toughness of tape-cast yttria-stabilized zirconia, Journal of the American Ceramic Society, 83 (2000) 2029-2035.

[9] A. Atkinson, A. Selçuk, Mechanical behavior of ceramic oxygen ion-conducting membranes, Solid State Ionics, 134 (2000) 59-66.

[10] ] H. Toftegaard, B.F. Sørensen, S. Linderoth, M. Lundberg, S. Feih, Effects of heat-treatments on the mechanical strength of coated YSZ: an experimental assessment, Journal of the American Ceramic Society, 92 (2009) 2704-2712.

[11] M. Pihlatie, A. Kaiser, M. Mogensen, Mechanical properties of NiO/Ni-YSZ composites depending on temperature, porosity and redox cycling, Journal of the European Ceramic Society, 29 (2009) 1657-1664.

[12] S. Giraud, J. Canel, Young's modulus of some SOFCs materials as a function of temperature, Journal of the European Ceramic Society, 28 (2008) 77-83.

[13] T. Zhang, Q. Zhu, W.L. Huang, Z. Xie, X. Xin, Stress field and failure probability analysis for the single cell of planar solid oxide fuel cells, Journal of Power Sources, 182 (2008) 540-545.

[14] J. Laurencin, G. Delette, F. Lefebvre-Joud, M. Dupeux, A numerical tool to estimate SOFC mechanical degradation: case of planar cell configuration, Journal of the European Ceramic Society, 28 (2008) 1857-1869.

[15] S. Pitakthapanaphong, E. Busso, Finite element analysis of the fracture behavior of multi-layered systems used in solid oxide fuel cell applications, Modelling and Simulation in Materials Science and Engineering, 13 (2005) 531.
[16] J. Johnson, J. Qu, Effective modulus and coefficient of thermal expansion of Ni-YSZ porous cermets, Journal of Power Sources, 181 (2008) 85-92.
[17] X. Liu, C.L. Martin, D. Bouvard, S. Di Iorio, J. Laurencin, G. Delette, Strength of highly porous ceramic electrodes, Journal of the American Ceramic Society, 94 (2011) 3500-3508.
[18] S. Kakac, A. Pramuanjaroenkij, X.Y. Zhou, A review of numerical modeling of solid oxide fuel cells, International Journal of Hydrogen Energy, 32 (2007) 761-786.
[19] J.R. Wilson, W. Kobsiriphat, R. Mendoza, H. Chen, J.M. Hiller, D.J. Miller, K. Thornton, P.W. Voorhees, S.B. Adler, S.A. Barnett, Three-dimensional reconstruction of a solid-oxide fuel-cell anode, Nature Materials, 5 (2006) 541-544.
[20] J.R. Wilson, A.T. Duong, M. Gameiro, H. Chen, K. Thornton, D.R. Mumm, S.A. Barnett, Quantitative three-dimensional microstructure of a solid oxide fuel cell cathode, Electrochemistry Communications, 11 (2009) 1052-1056.
[21] W. Weibull, A statistical distribution of wide applicability, Journal of Applied Mechanics, 18 (1951) 293-297.
[22] S. Vaidya, J.-H. Kim, Continuum Mechanics of Solid Oxide Fuel Cells Using Three-Dimensional Reconstructed Microstructures, in: Y.X. Gan (Ed.), Continuum Mechanics - Progress in Fundamentals and Engineering Applications, InTech, Rijeka, 2012, pp. 73-88.
[23] J. Kramer, D. Mastronarde, J. McIntosh, Computer visualization of three dimensional image data using IMOD, Journal of Structural Biology, 116 (1996) 71-76.
[24] Abaqus v6.9 User's Manual, Dassault Systemes Simulia Corp., Providence, Rhode Island.
[25] MATLAB ® 2010a, The MathWorks, Inc., Natick, Massachusetts.
[26] F. Ebrahimi, G. Bourne, M.S. Kelly, T. Matthews, Mechanical properties of nanocrystalline nickel produced by electrodeposition, Nanostructured Materials, 11 (1999) 343-350.
[27] M. Meyers, K. Chawla, Mechanical Behavior of Materials, Prentice Hall, Upper Saddle River, New Jersey; 1999.
[28] S. Vaidya, J.-H. Kim, Finite element thermal stress analysis of solid oxide fuel cell cathode microstructures, Journal of Power Sources, 225 (2013) 269-276.
[29] W. Zhu, D. Ding, C. Xia, Enhancement in three-phase boundary of SOFC electrodes by an ion impregnation method: a modeling comparison, Electrochemical and Solid-State Letters, 11 (2008) B83-B86.

[30] N. Vivet, S. Chupin, E. Estrade, A. Richard, S. Bonnamy, D. Rochais, E. Bruneton, Effect of Ni content in SOFC Ni-YSZ cermets: A three-dimensional study by FIB-SEM tomography, Journal of Power Sources, 196 (2011) 9989-9997.
[31] Abaqus v6.11 User's Manual, Dassault Systemes Simulia Corp., Providence, Rhode Island.
[32] J. Xiao, H. Schneider, C. Dönnecke, G. König, Wedge splitting test on fracture behaviour of ultra high strength concrete, Construction and Building Materials, 18 (2004) 359-365.
[33] B.N. Nguyen, B.J. Koeppel, S. Ahzi, M.A. Khaleel, P. Singh, Crack growth in solid oxide fuel cell materials: from discrete to continuum damage modeling, Journal of the American Ceramic Society, 89 (2006) 1358-1368.
[34] M. Janssen, J. Zuidema, R. J. H. Wanhill, Fracture Mechanics, 2nd Edition, VSSD; 2006.
[35] T.L. Anderson, Fracture Mechanics: Fundamentals and Applications, 4th Edition, CRC press; 2005.
[36] L. Liu, G.-Y. Kim, A. Chandra, Modeling of thermal stresses and lifetime prediction of planar solid oxide fuel cell under thermal cycling conditions, Journal of Power Sources, 195 (2010) 2310-2318.
[37] C.M. Dikwal, W. Bujalski, K. Kendall, The effect of temperature gradients on thermal cycling and isothermal ageing of micro-tubular solid oxide fuel cells, Journal of Power Sources, 193 (2009) 241-248.
[38] W. Bujalski, J. Paragreen, G. Reade, S. Pyke, K. Kendall, Cycling studies of solid oxide fuel cells, Journal of Power Sources, 157 (2006) 745-749.

# Appendix

Computer program for reconstruction of three-dimensional finite element cathode microstructure model from a stack of two-dimensional microstructure images

```
% Author: Sushrut Sanjiv Vaidya
% ------------------------------------------------------------------------
% A MATLAB program that reads in a series of TIFF images of a 2-D SOFC cathode
% microstructure (50:50 wt. % LSM:YSZ), simplifies each image by pixel square analysis,
% converts the pixel matrices into a 3-D model, and then writes an Abaqus input file to analyze the
% response of the 3D microstructure to a thermal load (spatially uniform temperature field).
% Note: Pixel value 255 => LSM
%       Pixel value 127 => YSZ
%       Pixel value 0   => pores
%------------------------------------------------------------------------
% Program starts here
% Reading of the original 2-D cathode microstructure images, and storage as 2-D pixel arrays

clear
clc

original_image1 = imread('image1.tif', 'tif');
original_image2 = imread('image2.tif', 'tif');
original_image3 = imread('image3.tif', 'tif');
original_image4 = imread('image4.tif', 'tif');
original_image5 = imread('image5.tif', 'tif');
original_image6 = imread('image6.tif', 'tif');
original_image7 = imread('image7.tif', 'tif');
original_image8 = imread('image8.tif', 'tif');
original_image9 = imread('image9.tif', 'tif');
original_image10 = imread('image10.tif', 'tif');
original_image11 = imread('image11.tif', 'tif');
original_image12 = imread('image12.tif', 'tif');
original_image13 = imread('image13.tif', 'tif');
original_image14 = imread('image14.tif', 'tif');
original_image15 = imread('image15.tif', 'tif');
```

```
original_image16 = imread('image16.tif', 'tif');
original_image17 = imread('image17.tif', 'tif');
original_image18 = imread('image18.tif', 'tif');
original_image19 = imread('image19.tif', 'tif');
original_image20 = imread('image20.tif', 'tif');
original_image21 = imread('image21.tif', 'tif');
original_image22 = imread('image22.tif', 'tif');
original_image23 = imread('image23.tif', 'tif');
original_image24 = imread('image24.tif', 'tif');
original_image25 = imread('image25.tif', 'tif');
original_image26 = imread('image26.tif', 'tif');
original_image27 = imread('image27.tif', 'tif');
original_image28 = imread('image28.tif', 'tif');
original_image29 = imread('image29.tif', 'tif');
original_image30 = imread('image30.tif', 'tif');
original_image31 = imread('image31.tif', 'tif');
original_image32 = imread('image32.tif', 'tif');
original_image33 = imread('image33.tif', 'tif');
original_image34 = imread('image34.tif', 'tif');
original_image35 = imread('image35.tif', 'tif');
original_image36 = imread('image36.tif', 'tif');
original_image37 = imread('image37.tif', 'tif');
original_image38 = imread('image38.tif', 'tif');
original_image39 = imread('image39.tif', 'tif');
original_image40 = imread('image40.tif', 'tif');
original_image41 = imread('image41.tif', 'tif');

% Image reading and storage ends here

% Total number of images used = (n_image_planes) = 41

[rows columns] = size(original_image1);      % Determination of size of original image

n = 81;      % Total number of (image+buffer) planes in 3-D model = (2*n_image_planes-1)
```

```
% Generation of a stack of 2-D images using a cell array {} data structure
im_arr_or = {original_image1 original_image2 original_image3 original_image4 original_image5…
original_image6 original_image7 original_image8 original_image9 original_image10…
original_image11 original_image12 original_image13 original_image14 original_image15...
original_image16 original_image17 original_image18 original_image19 original_image20…
original_image21 original_image22 original_image23 original_image24 original_image25…
original_image26 original_image27 original_image28 original_image29 original_image30…
original_image31 original_image32 original_image33 original_image34 original_image35…
original_image36 original_image37 original_image38 original_image39 original_image40
original_image41};
% Assignment of initial and final row and column numbers for extracting pixel array subset from
% original pixel array. Assignment of row and column increments for analyzing (2 x 2) pixel
% squares
row_i = 2;
row_f = rows;
row_incr = 2;
col_i = 23;
col_f = 194;
col_incr = 2;
% Image simplification: Analysis of (2 x 2) pixel squares of original image to derive simplified
% image
for counter_len = 1:length(im_arr_or)
   for counter_rows = row_i:row_incr:(row_f-1)
      for counter_columns = col_i:col_incr:(col_f-1)
         counterLSM = 0;
         counterYSZ = 0;
         counterPore = 0;
         if im_arr_or{counter_len}(counter_rows,counter_columns) = = 255
            counterLSM = counterLSM+1;
         elseif im_arr_or{counter_len}(counter_rows,counter_columns) = = 127
            counterYSZ = counterYSZ+1;
         elseif im_arr_or{counter_len}(counter_rows,counter_columns) = = 0
            counterPore = counterPore+1;
         end
```

```
if im_arr_or{counter_len}(counter_rows,counter_columns+1) = = 255
   counterLSM = counterLSM+1;
elseif im_arr_or{counter_len}(counter_rows,counter_columns+1) = = 127
   counterYSZ = counterYSZ+1;
elseif im_arr_or{counter_len}(counter_rows,counter_columns+1) = = 0
   counterPore = counterPore+1;
end
if im_arr_or{counter_len}(counter_rows+1,counter_columns) = = 255
   counterLSM = counterLSM+1;
elseif im_arr_or{counter_len}(counter_rows+1,counter_columns) = = 127
   counterYSZ = counterYSZ+1;
elseif im_arr_or{counter_len}(counter_rows+1,counter_columns) = = 0
   counterPore = counterPore+1;
end
if im_arr_or{counter_len}(counter_rows+1,counter_columns+1) = = 255
   counterLSM = counterLSM+1;
elseif im_arr_or{counter_len}(counter_rows+1,counter_columns+1) = = 127
   counterYSZ = counterYSZ+1;
elseif im_arr_or{counter_len}(counter_rows+1,counter_columns+1) = = 0
   counterPore = counterPore+1;
end
c_phase_f = max([counterLSM counterYSZ counterPore]);
if (c_phase_f = = counterLSM && c_phase_f ~= counterYSZ && c_phase_f ~= counterPore)
   c_phase_ff = counterLSM;
   phase_ff = 255;
elseif (c_phase_f = = counterYSZ && c_phase_f ~= counterPore && c_phase_f ~= counterLSM)
   c_phase_ff = counterYSZ;
   phase_ff = 127;
elseif (c_phase_f = = counterPore && c_phase_f ~= counterLSM && c_phase_f ~= counterYSZ)
   c_phase_ff = counterPore;
   phase_ff = 0;
elseif (c_phase_f = = counterLSM && c_phase_f = = counterYSZ && c_phase_f ~= counterPore)
   c_phase_ff = counterYSZ;
   phase_ff = 127;
```

```
        elseif (c_phase_f = = counterYSZ && c_phase_f = = counterPore && c_phase_f ~= counterLSM)
           c_phase_ff = counterYSZ;
           phase_ff = 127;
        elseif (c_phase_f = = counterPore && c_phase_f = = counterLSM && c_phase_f ~= counterYSZ)
           c_phase_ff = counterLSM;
           phase_ff = 255;
        end
im_arr_mod{counter_len}((counter_rows-row_i)/row_incr+1,(counter_columns-col_i)/col_incr+1) =
phase_ff;
      end
   end
end

[rows_red columns_red] = size(im_arr_mod{1});  % Determination of size of simplified image

% Input file starts here

outputfile_id = fopen('cathode5050_2by2_fx_temp_dep_800.txt', 'w');
fprintf(outputfile_id, '*Heading\r');
fprintf(outputfile_id, '\nCathode three dimensional microstructure\r');

fprintf(outputfile_id, '\n**\r');
fprintf(outputfile_id, '\n**\t\tOUTPUT CONTROL INSTRUCTIONS\t\t**\r');
fprintf(outputfile_id, '\n*Preprint, echo=NO, history=NO, model=NO\r');

fprintf(outputfile_id, '\n**\r');
fprintf(outputfile_id, '\n**\t\tNODE DEFINITION\t\t**\r');
fprintf(outputfile_id, '\n*Node\r');
```

**% Node numbering algorithm starts**

```
for counter_z = 1:n
   for counter_horizontal = 1:(rows_red+1)
      for counter_vertical = 1:(columns_red+1)
         node_number = (rows_red+1)*(columns_red+1)*(counter_z-1) + (columns_red+1) *
(counter_horizontal-1) + counter_vertical;
         x_coordinate = (counter_vertical-1)*(2*40.8*10^(-6));
         y_coordinate = ((rows_red+1)-counter_horizontal)*(2*40.8*10^(-6));
         z_coordinate = (counter_z-1)*(53.3*10^(-6));
         fprintf(outputfile_id, '\n%d, %f, %f, %f\r', node_number, x_coordinate, y_coordinate,
z_coordinate);
      end
   end
end

fprintf(outputfile_id, '\n*Nset, nset=ENTIRE_CATHODE\r');

for counter_z = 1:n
   for counter_horizontal = 1:(rows_red+1)
      for counter_vertical = 1:(columns_red+1)
         node_number = (rows_red+1)*(columns_red+1)*(counter_z-1) + (columns_red+1) *
(counter_horizontal-1) + counter_vertical;
         fprintf(outputfile_id, '\n%d,\r', node_number);
      end
   end
end
```

**% Node numbering algorithm ends**

**% Element numbering and node ordering algorithm. Assignment of solid elements to LSM element % set based on pixel value (255).**

```
fprintf(outputfile_id, '\n**\r');
fprintf(outputfile_id, '\n**\t\tELEMENT DEFINITION\t\t**\r');
fprintf(outputfile_id, '\n*Element, type=C3D8, elset=LSM\r');
for counter_len = 1:length(im_arr_mod)
   if counter_len = = 1
      z_factor = 2*counter_len-2;
       for counter_rows = 1:rows_red
         for counter_columns = 1:columns_red
           if im_arr_mod{counter_len}(counter_rows, counter_columns) = = 255
              element_number = rows_red*columns_red*z_factor+columns_red*(counter_rows-1) +
counter_columns;
              node1 = (rows_red+1)*(columns_red+1)*z_factor+(columns_red+1)*(counter_rows-1) +
counter_columns;
              node2 = (rows_red+1) * (columns_red+1) * z_factor + (columns_red+1) * counter_rows +
counter_columns;
              node3 = (rows_red+1) * (columns_red+1) * z_factor + (columns_red+1) * counter_rows +
(counter_columns+1);
              node4 = (rows_red+1)*(columns_red+1)*z_factor+(columns_red+1)*(counter_rows-1) +
(counter_columns+1);
              node5 = (rows_red+1)*(columns_red+1)*(z_factor+1)+(columns_red+1)*(counter_rows-1) +
counter_columns;
              node6 = (rows_red+1) * (columns_red+1) * (z_factor+1) + (columns_red+1) * counter_rows +
counter_columns;
              node7 = (rows_red+1) * (columns_red+1) * (z_factor+1) + (columns_red+1) * counter_rows +
(counter_columns+1);
              node8 = (rows_red+1)*(columns_red+1)*(z_factor+1)+(columns_red+1)*(counter_rows-1) +
(counter_columns+1);
fprintf(outputfile_id, '\n%d, %d, %d, %d, %d, %d, %d, %d, %d\r', element_number, node1, node2,
node3, node4, node5, node6, node7, node8);
            end
          end
        end
```

```
   elseif counter_len = = length(im_arr_mod)
          z_factor = 2*counter_len-3;
           for counter_rows = 1:rows_red
             for counter_columns = 1:columns_red
               if im_arr_mod{counter_len}(counter_rows, counter_columns) = = 255
                  element_number = rows_red*columns_red*z_factor+columns_red*(counter_rows-1) +
counter_columns;
                  node1 = (rows_red+1)*(columns_red+1)*z_factor+(columns_red+1)*(counter_rows-1) +
counter_columns;
                  node2 = (rows_red+1) * (columns_red+1) * z_factor + (columns_red+1) * counter_rows +
counter_columns;
                  node3 = (rows_red+1) * (columns_red+1) * z_factor + (columns_red+1) * counter_rows +
(counter_columns+1);
                  node4 = (rows_red+1)*(columns_red+1)*z_factor+(columns_red+1)*(counter_rows-1) +
(counter_columns+1);
                  node5 = (rows_red+1)*(columns_red+1)*(z_factor+1)+(columns_red+1)*(counter_rows-1)
+ counter_columns;
                  node6 = (rows_red+1) * (columns_red+1) * (z_factor+1) + (columns_red+1) * counter_rows
+ counter_columns;
                  node7 = (rows_red+1) * (columns_red+1) * (z_factor+1) + (columns_red+1) * counter_rows
+ (counter_columns+1);
                  node8 = (rows_red+1)*(columns_red+1)*(z_factor+1)+(columns_red+1)*(counter_rows-1)
+ (counter_columns+1);
fprintf(outputfile_id, '\n%d, %d, %d, %d, %d, %d, %d, %d, %d\r', element_number, node1, node2,
node3, node4, node5, node6, node7, node8);
               end
             end
           end
```

```
else
        z_factor1 = 2*counter_len-3;
        z_factor2 = 2*counter_len-2;
         for counter_rows = 1:rows_red
           for counter_columns = 1:columns_red
             if im_arr_mod{counter_len}(counter_rows, counter_columns) = = 255
              element_number_1 = rows_red*columns_red*z_factor1+columns_red*(counter_rows-1) +
counter_columns;
              node1_1 = (rows_red+1)*(columns_red+1)*z_factor1+(columns_red+1)*(counter_rows-1) +
counter_columns;
              node2_1 = (rows_red+1) * (columns_red+1) * z_factor1 + (columns_red+1) * counter_rows +
counter_columns;
              node3_1 = (rows_red+1) * (columns_red+1) * z_factor1 + (columns_red+1) * counter_rows +
(counter_columns+1);
              node4_1 = (rows_red+1)*(columns_red+1)*z_factor1+(columns_red+1)*(counter_rows-1) +
(counter_columns+1);
             node5_1 = (rows_red+1)*(columns_red+1)*(z_factor1+1)+(columns_red+1)*(counter_rows-1)
+ counter_columns;
             node6_1 = (rows_red+1) * (columns_red+1) * (z_factor1+1) + (columns_red+1) *
counter_rows + counter_columns;
             node7_1 = (rows_red+1) * (columns_red+1) * (z_factor1+1) + (columns_red+1) *
counter_rows + (counter_columns+1);
             node8_1 = (rows_red+1)*(columns_red+1)*(z_factor1+1)+(columns_red+1)*(counter_rows-1)
+ (counter_columns+1);
             element_number_2 = rows_red*columns_red*z_factor2+columns_red*(counter_rows-1) +
counter_columns;
             node1_2 = (rows_red+1)*(columns_red+1)*z_factor2+(columns_red+1)*(counter_rows-1) +
counter_columns;
             node2_2 = (rows_red+1) * (columns_red+1) * z_factor2 + (columns_red+1) * counter_rows +
counter_columns;
             node3_2 = (rows_red+1) * (columns_red+1) * z_factor2 + (columns_red+1) * counter_rows +
(counter_columns+1);
             node4_2 = (rows_red+1)*(columns_red+1)*z_factor2+(columns_red+1)*(counter_rows-1) +
(counter_columns+1);
```

```
            node5_2 = (rows_red+1)*(columns_red+1)*(z_factor2+1)+(columns_red+1)*(counter_rows-1)
+ counter_columns;
            node6_2 = (rows_red+1) * (columns_red+1) * (z_factor2+1) + (columns_red+1) *
counter_rows + counter_columns;
            node7_2 = (rows_red+1) * (columns_red+1) * (z_factor2+1) + (columns_red+1) *
counter_rows + (counter_columns+1);
            node8_2 = (rows_red+1)*(columns_red+1)*(z_factor2+1)+(columns_red+1)*(counter_rows-1)
+ (counter_columns+1);
fprintf(outputfile_id, '\n%d, %d, %d, %d, %d, %d, %d, %d, %d\r', element_number_1, node1_1,
node2_1, node3_1, node4_1, node5_1, node6_1, node7_1, node8_1);
fprintf(outputfile_id, '\n%d, %d, %d, %d, %d, %d, %d, %d, %d\r', element_number_2, node1_2,
node2_2, node3_2, node4_2, node5_2, node6_2, node7_2, node8_2);
             end
           end
         end
   end
end
```

**% Element numbering and node ordering algorithm. Assignment of solid elements to YSZ element**
**% set based on pixel value (127).**

```
fprintf(outputfile_id, '\n**\r');
fprintf(outputfile_id, '\n*Element, type=C3D8, elset=YSZ\r');
for counter_len = 1:length(im_arr_mod)
   if counter_len = = 1
      z_factor = 2*counter_len-2;
       for counter_rows = 1:rows_red
         for counter_columns = 1:columns_red
          if im_arr_mod{counter_len}(counter_rows, counter_columns) = = 127
           element_number = rows_red*columns_red*z_factor+columns_red*(counter_rows-1) +
counter_columns;
           node1 = (rows_red+1)*(columns_red+1)*z_factor+(columns_red+1)*(counter_rows-1) +
counter_columns;
           node2 = (rows_red+1) * (columns_red+1) * z_factor + (columns_red+1) * counter_rows +
counter_columns;
```

```
            node3 = (rows_red+1) * (columns_red+1) * z_factor + (columns_red+1) * counter_rows +
(counter_columns+1);
            node4 = (rows_red+1)*(columns_red+1)*z_factor+(columns_red+1)*(counter_rows-1) +
(counter_columns+1);
            node5 = (rows_red+1)*(columns_red+1)*(z_factor+1)+(columns_red+1)*(counter_rows-1) +
counter_columns;
            node6 = (rows_red+1) * (columns_red+1) * (z_factor+1) + (columns_red+1) * counter_rows +
counter_columns;
            node7 = (rows_red+1) * (columns_red+1) * (z_factor+1) + (columns_red+1) * counter_rows +
(counter_columns+1);
            node8 = (rows_red+1)*(columns_red+1)*(z_factor+1)+(columns_red+1)*(counter_rows-1) +
(counter_columns+1);
fprintf(outputfile_id, '\n%d, %d, %d, %d, %d, %d, %d, %d, %d\r', element_number, node1, node2,
node3, node4, node5, node6, node7, node8);
          end
        end
      end
  elseif counter_len = = length(im_arr_mod)
        z_factor = 2*counter_len-3;
         for counter_rows = 1:rows_red
           for counter_columns = 1:columns_red
             if im_arr_mod{counter_len}(counter_rows, counter_columns) = = 127
              element_number = rows_red*columns_red*z_factor+columns_red*(counter_rows-1) +
counter_columns;
              node1 = (rows_red+1)*(columns_red+1)*z_factor+(columns_red+1)*(counter_rows-1) +
counter_columns;
              node2 = (rows_red+1) * (columns_red+1) * z_factor + (columns_red+1) * counter_rows +
counter_columns;
              node3 = (rows_red+1) * (columns_red+1) * z_factor + (columns_red+1) * counter_rows +
(counter_columns+1);
              node4 = (rows_red+1)*(columns_red+1)*z_factor+(columns_red+1)*(counter_rows-1) +
(counter_columns+1);
              node5 = (rows_red+1)*(columns_red+1)*(z_factor+1)+(columns_red+1)*(counter_rows-1) +
counter_columns;
```

```
            node6 = (rows_red+1) * (columns_red+1) * (z_factor+1) + (columns_red+1) * counter_rows
+ counter_columns;
            node7 = (rows_red+1) * (columns_red+1) * (z_factor+1) + (columns_red+1) * counter_rows
+ (counter_columns+1);
            node8 = (rows_red+1)*(columns_red+1)*(z_factor+1)+(columns_red+1)*(counter_rows-1) +
(counter_columns+1);
fprintf(outputfile_id, '\n%d, %d, %d, %d, %d, %d, %d, %d, %d\r', element_number, node1, node2,
node3, node4, node5, node6, node7, node8);
          end
        end
      end
  else
      z_factor1 = 2*counter_len-3;
      z_factor2 = 2*counter_len-2;
       for counter_rows = 1:rows_red
         for counter_columns = 1:columns_red
          if im_arr_mod{counter_len}(counter_rows, counter_columns) = = 127
           element_number_1 = rows_red*columns_red*z_factor1+columns_red*(counter_rows-1) +
counter_columns;
            node1_1 = (rows_red+1)*(columns_red+1)*z_factor1+(columns_red+1)*(counter_rows-1) +
counter_columns;
            node2_1 = (rows_red+1) * (columns_red+1) * z_factor1 + (columns_red+1) * counter_rows +
counter_columns;
            node3_1 = (rows_red+1) * (columns_red+1) * z_factor1 + (columns_red+1) * counter_rows +
(counter_columns+1);
            node4_1 = (rows_red+1)*(columns_red+1)*z_factor1+(columns_red+1)*(counter_rows-1) +
(counter_columns+1);
            node5_1 = (rows_red+1)*(columns_red+1)*(z_factor1+1)+(columns_red+1)*(counter_rows-1)
+ counter_columns;
            node6_1 = (rows_red+1) * (columns_red+1) * (z_factor1+1) + (columns_red+1) *
counter_rows + counter_columns;
            node7_1 = (rows_red+1) * (columns_red+1) * (z_factor1+1) + (columns_red+1) *
counter_rows + (counter_columns+1);
```

```
            node8_1 = (rows_red+1)*(columns_red+1)*(z_factor1+1)+(columns_red+1)*(counter_rows-1)
+ (counter_columns+1);
             element_number_2 = rows_red*columns_red*z_factor2+columns_red*(counter_rows-1) +
counter_columns;
            node1_2 = (rows_red+1)*(columns_red+1)*z_factor2+(columns_red+1)*(counter_rows-1) +
counter_columns;
            node2_2 = (rows_red+1) * (columns_red+1) * z_factor2 + (columns_red+1) * counter_rows +
counter_columns;
            node3_2 = (rows_red+1) * (columns_red+1) * z_factor2 + (columns_red+1) * counter_rows +
(counter_columns+1);
            node4_2 = (rows_red+1)*(columns_red+1)*z_factor2+(columns_red+1)*(counter_rows-1) +
(counter_columns+1);
            node5_2 = (rows_red+1)*(columns_red+1)*(z_factor2+1)+(columns_red+1)*(counter_rows-1)
+ counter_columns;
            node6_2 = (rows_red+1) * (columns_red+1) * (z_factor2+1) + (columns_red+1) *
counter_rows + counter_columns;
            node7_2 = (rows_red+1) * (columns_red+1) * (z_factor2+1) + (columns_red+1) *
counter_rows + (counter_columns+1);
            node8_2 = (rows_red+1)*(columns_red+1)*(z_factor2+1)+(columns_red+1)*(counter_rows-1)
+ (counter_columns+1);
fprintf(outputfile_id, '\n%d, %d, %d, %d, %d, %d, %d, %d, %d\r', element_number_1, node1_1,
node2_1, node3_1, node4_1, node5_1, node6_1, node7_1, node8_1);
fprintf(outputfile_id, '\n%d, %d, %d, %d, %d, %d, %d, %d, %d\r', element_number_2, node1_2,
node2_2, node3_2, node4_2, node5_2, node6_2, node7_2, node8_2);
             end
           end
         end
   end
end
```

**% Element numbering, node ordering, and element set assignment algorithms for LSM and YSZ % element sets end here.**

**% Assignment of solid sections and material definitions to LSM and YSZ element sets**

```
fprintf(outputfile_id, '\n**\r');
fprintf(outputfile_id, '\n**\t\tSOLID SECTION DEFINITION FOR NODE SETS\t\t**\r');
fprintf(outputfile_id, '\n*Solid Section, material=LSM, elset=LSM\r');
fprintf(outputfile_id, '\n**\r');
fprintf(outputfile_id, '\n*Solid Section, material=YSZ, elset=YSZ\r');
```

**% Definition of temperature-dependent material properties for LSM and YSZ**

```
fprintf(outputfile_id, '\n**\r');
fprintf(outputfile_id, '\n**\t\tMATERIAL PROPERTIES DEFINITION\t\t**\r');
fprintf(outputfile_id, '\n*Material, name=LSM\r');
fprintf(outputfile_id, '\n*Elastic\r');
fprintf(outputfile_id, '\n40E3, 0.25, 0\r');
fprintf(outputfile_id, '\n40E3, 0.25, 350\r');
fprintf(outputfile_id, '\n42E3, 0.25, 400\r');
fprintf(outputfile_id, '\n46E3, 0.25, 500\r');
fprintf(outputfile_id, '\n48E3, 0.25, 600\r');
fprintf(outputfile_id, '\n48E3, 0.25, 800\r');
fprintf(outputfile_id, '\n*Expansion\r');
fprintf(outputfile_id, '\n11.4E-6\r');
fprintf(outputfile_id, '\n**\r');
fprintf(outputfile_id, '\n*Material, name=YSZ\r');
fprintf(outputfile_id, '\n*Elastic\r');
fprintf(outputfile_id, '\n205E3, 0.3, 20\r');
fprintf(outputfile_id, '\n200.5E3, 0.3, 100\r');
fprintf(outputfile_id, '\n192E3, 0.3, 200\r');
fprintf(outputfile_id, '\n174E3, 0.3, 300\r');
fprintf(outputfile_id, '\n155E3, 0.3, 400\r');
fprintf(outputfile_id, '\n138E3, 0.3, 500\r');
fprintf(outputfile_id, '\n135E3, 0.3, 600\r');
fprintf(outputfile_id, '\n140E3, 0.3, 700\r');
fprintf(outputfile_id, '\n147.5E3, 0.3, 800\r');
fprintf(outputfile_id, '\n*Expansion\r');
fprintf(outputfile_id, '\n8.2E-6,0\r');
fprintf(outputfile_id, '\n10E-6,800\r');
```

**% Node set definitions for the 6 faces of the cathode model for assigning fixed boundary conditions**

```
fprintf(outputfile_id, '\n*Nset, nset=FACE_ONE\r');
for counter_z = 1:n
   for counter_rows = 1:(rows_red+1)
      node_no = (rows_red+1)*(columns_red+1)*(counter_z-1)+(columns_red+1)*(counter_rows-1)+1;
      fprintf(outputfile_id, '\n%d,\r', node_no);
   end
end

fprintf(outputfile_id, '\n*Nset, nset=FACE_TWO\r');
for counter_rows = 1:(rows_red+1)
   for counter_columns = 1:(columns_red+1)
      node_no = (rows_red+1)*(columns_red+1)*(n-1)+(columns_red+1)*(counter_rows-1) +
counter_columns;
      fprintf(outputfile_id, '\n%d,\r', node_no);
   end
end

fprintf(outputfile_id, '\n*Nset, nset=FACE_THREE\r');
for counter_z = 1:n
   for counter_rows = 1:(rows_red+1)
      node_no = (rows_red+1)*(columns_red+1)*(counter_z-1)+(columns_red+1)*(counter_rows-1) +
(columns_red+1);
      fprintf(outputfile_id, '\n%d,\r', node_no);
   end
end

fprintf(outputfile_id, '\n*Nset, nset=FACE_FOUR\r');
for counter_rows = 1:(rows_red+1)
   for counter_columns = 1:(columns_red+1)
      node_no = (columns_red+1)*(counter_rows-1)+counter_columns;
      fprintf(outputfile_id, '\n%d,\r', node_no);
   end
end
```

```
fprintf(outputfile_id, '\n*Nset, nset=FACE_FIVE\r');
for counter_z = 1:n
   for counter_columns = 1:(columns_red+1)
      node_no = (rows_red+1)*(columns_red+1)*(counter_z-1)+counter_columns;
      fprintf(outputfile_id, '\n%d,\r', node_no);
   end
end

fprintf(outputfile_id, '\n*Nset, nset=FACE_SIX\r');
for counter_z = 1:n
   for counter_columns = 1:(columns_red+1)
      node_no = (rows_red+1)*(columns_red+1)*(counter_z-1) + (columns_red+1) * rows_red +
counter_columns;
      fprintf(outputfile_id, '\n%d,\r', node_no);
   end
end

% Definition of analysis step, boundary conditions, initial temperature, and operating temperature
% field
fprintf(outputfile_id, '\n**\r');
fprintf(outputfile_id, '\n**\t\tSTEP DEFINITION (LOADING & RESPONSE)\t\t**\r');
fprintf(outputfile_id, '\n*Step\r');
fprintf(outputfile_id, '\n*Static\r');
fprintf(outputfile_id, '\n1.0, 1.0\r');
fprintf(outputfile_id, '\n**\r');
```

```
fprintf(outputfile_id, '\n**\t\tBOUNDARY CONDITION DEFINITION\t\t**\r');
fprintf(outputfile_id, '\n*Boundary\r');
fprintf(outputfile_id, '\nFACE_ONE, ENCASTRE\r');
fprintf(outputfile_id, '\n*Boundary\r');
fprintf(outputfile_id, '\nFACE_TWO, ENCASTRE\r');
fprintf(outputfile_id, '\n*Boundary\r');
fprintf(outputfile_id, '\nFACE_THREE, ENCASTRE\r');
fprintf(outputfile_id, '\n*Boundary\r');
fprintf(outputfile_id, '\nFACE_FOUR, ENCASTRE\r');
fprintf(outputfile_id, '\n*Boundary\r');
fprintf(outputfile_id, '\nFACE_FIVE, ENCASTRE\r');
fprintf(outputfile_id, '\n*Boundary\r');
fprintf(outputfile_id, '\nFACE_SIX, ENCASTRE\r');
fprintf(outputfile_id, '\n*Initial Conditions, type=TEMPERATURE\r');
fprintf(outputfile_id, '\nENTIRE_CATHODE, 20\r');
fprintf(outputfile_id, '\n*Temperature\r');
fprintf(outputfile_id, '\nENTIRE_CATHODE, 820\r');
```

**% Definition of output requests for centroidal principal stresses from LSM and YSZ element sets**

```
fprintf(outputfile_id, '\n*El Print, position=CENTROIDAL, elset=LSM\r');
fprintf(outputfile_id, '\nSP\r');
fprintf(outputfile_id, '\n*El Print, position=CENTROIDAL, elset=YSZ\r');
fprintf(outputfile_id, '\nSP\r');

fprintf(outputfile_id, '\n*End Step\r');
```

**% Input file ends here**

**% Program ends here**